All-sky search for continuous gravitational waves from isolated neutron stars in the early O3 LIGO data

R. Abbott *et al.*[*]
(LIGO Scientific Collaboration, Virgo Collaboration, and KAGRA Collaboration)

(Received 1 July 2021; accepted 16 September 2021; published 8 October 2021)

We report on an all-sky search for continuous gravitational waves in the frequency band 20–2000 Hz and with a frequency time derivative in the range of $[-1.0, +0.1] \times 10^{-8}$ Hz/s. Such a signal could be produced by a nearby, spinning and slightly nonaxisymmetric isolated neutron star in our Galaxy. This search uses the LIGO data from the first six months of Advanced LIGO's and Advanced Virgo's third observational run, O3. No periodic gravitational wave signals are observed, and 95% confidence-level (C.L.) frequentist upper limits are placed on their strengths. The lowest upper limits on worst-case (linearly polarized) strain amplitude h_0 are $\sim 1.7 \times 10^{-25}$ near 200 Hz. For a circularly polarized source (most favorable orientation), the lowest upper limits are $\sim 6.3 \times 10^{-26}$. These strict frequentist upper limits refer to all sky locations and the entire range of frequency derivative values. For a population-averaged ensemble of sky locations and stellar orientations, the lowest 95% C.L. upper limits on the strain amplitude are $\sim 1.4 \times 10^{-25}$. These upper limits improve upon our previously published all-sky results, with the greatest improvement (factor of ~ 2) seen at higher frequencies, in part because quantum squeezing has dramatically improved the detector noise level relative to the second observational run, O2. These limits are the most constraining to date over most of the parameter space searched.

DOI: 10.1103/PhysRevD.104.082004

I. INTRODUCTION

We report the results of an all-sky search for continuous, nearly monochromatic gravitational waves from rapidly rotating isolated neutron stars using the first six months of data from the third observing run (O3) of the Advanced Laser Interferometer Gravitational wave Observatory (Advanced LIGO [1,2]). This first search of the early O3 data uses the PowerFlux hierarchical search program [3–8] with loose-coherence follow-up [9,10] of outliers and covers a broad band of frequencies (20–2000 Hz) and frequency derivatives ($[-1.0, +0.1] \times 10^{-8}$ Hz/s). Although more than 1.4×10^5 search outliers are found in the initial stage of analysis, successive follow-up stages failed to confirm an astrophysical signal. Hence the primary results from this analysis are the upper limits on strain amplitude presented in Sec. IV A.

All-sky searches for continuous gravitational waves from isolated neutron stars have been carried out in Advanced LIGO and Virgo data previously [7,8,11–18]. The results presented here are the most sensitive to date in strain amplitude for a broadband, all-sky search with high allowed spin-down magnitudes, with improvement factors ranging from ~ 1.2 at signal frequencies of ~ 100 Hz to ~ 2 at the higher frequencies. The improvement with respect to similar, previous analyses of O2 data [12,13] is greater at higher frequencies, in part because of the improved detector noise (~ 3 db) achieved with quantum squeezing [19] and in part because longer Fourier transform coherence times are used here (for frequencies up to 1475 Hz) than in the O2 analyses.

Our primary targets in this analysis are fast-spinning, nonaxisymmetric neutron stars in the Milky Way. Given the immense pressure on its nuclear matter, one expects a neutron star to assume a highly spherical shape in the limit of no rotation and, with rotation, to form an axisymmetric oblate spheroid. A number of physical processes can disrupt the symmetry, however, to produce quadrupolar gravitational waves from the stellar rotation. Those processes include crustal distortions from cooling or accretion, buried magnetic field energy and excitation of r-modes. Comprehensive reviews of continuous gravitational wave emission mechanisms from neutron stars can be found in [20,21].

This article is organized as follows: Sec. II describes the dataset used, including steps taken to mitigate extremely loud and relatively frequent instrumental glitches seen in the O3 LIGO data, a phenomenon not seen in previous LIGO observing runs. Section III briefly describes the PowerFlux and loose-coherence algorithm used in this and previous searches. Section IV presents the results of the analysis. Section V concludes with a discussion of the results and prospects for future searches.

[*]Full author list given at the end of the article.

II. DATASETS USED

Advanced LIGO consists of two detectors, one in Hanford, Washington (designated H1), and the other in Livingston, Louisiana (designated L1), separated by a ∼3000-km baseline [1]. Each site hosts one, 4-km-long interferometer inside a vacuum envelope with the primary interferometer optics suspended by a cascaded, quadruple suspension system in order to isolate them from external disturbances. The interferometer mirrors act as test masses, and the passage of a gravitational wave induces a differential-arm length change that is proportional to the gravitational-wave strain amplitude.

Advanced LIGO's first observing run (O1) occurred between September 12, 2015 and January 19, 2016 and led to the discovery on September 14, 2015 of gravitational waves from binary black hole (BBH) coalescences [22]. The O2 observing run began November 30, 2016 and ended August 25, 2017 and included the first detection of a binary neutron star (BNS) merger [23]. The O3 run began April 1, 2019 and ended March 27, 2020, for which the first six months (April 1, 2019 to October 1, 2019), prior to a 1-month commissioning break, is designated as the O3a epoch. The analysis presented here is based primarily on the O3a dataset, with data from the remainder of the run (O3b epoch) used only for following up on promising signal candidates. From the O1, O2 and O3a datasets, the LIGO Scientific Collaboration and Virgo Collaboration have reported a total of 50 compact binary coalescences [24–26], primarily BBH events, with two binary neutron star (BNS) detections [23,27] and one potential binary neutron star / black hole detection [28].

The Virgo interferometer [29] observed during August 2017 near the end of the O2 run and throughout the O3 run. The Virgo data have not been used in this analysis, however, because of an unattractive tradeoff in computational cost for sensitivity gain, given the interferometer's higher noise level during the O3 run.

Prior to searching the O3a data for continuous wave (CW) signals, the quality of the data was assessed and steps taken to mitigate the effects of instrumental artifacts. As in previous Advanced LIGO observing runs [30], instrumental "lines" (sharp peaks in fine-resolution run-averaged H1 and L1 spectra) are marked, and where possible, their instrumental or environmental sources identified [31]. The resulting database of artifacts proved helpful in eliminating spurious signal candidates emerging from the search. In general, the line multiplicity for H1 O3a data was similar to that observed in the O2 run, while the line multiplicity for L1 O3a data was substantially reduced.

Another type of artifact observed in the O3a data for both H1 and L1 was relatively frequent and contained loud "glitches" (short, high-amplitude instrumental transients) with most of their spectral power lying below ∼500 Hz. Although loud glitches have been observed in previous runs, their frequency in O3a was dramatically higher. At present, investigations of the source of these glitches remain inconclusive. An effort to identify and mitigate them during the October 2019 commissioning break (between the O3a and O3b epochs) did not succeed. Unlike in previous LIGO data runs, the sheer spectral power in the glitches increased the effective broadband noise floor of the data below ∼500 Hz quite substantially, as seen in run-averaged spectra computed from 1800s and 7200s discrete Fourier transforms known as "SFTs" (for "short Fourier transforms"). Most CW searches based on summing strain spectral power from SFTs, including the PowerFlux program used here, apply weightings that disfavor SFTs with high noise. Because the average time interval between loud glitches in O3a data is comparable to or smaller than the coherence time of the SFTs; however, inverse noise weighting of SFTs proved much less effective than in previous runs, especially for the 7200s SFTs.

To mitigate the effects of these glitches on O3a CW searches for signals below 475 Hz, a simple glitch-gating algorithm was applied [32,33] to excise the transients from the data. For each 1/16-second for which a whitened version of the H1 and L1 strain data channels had excess rms power in the 25–50 Hz or 70–110 Hz bands, the strain channel was set to zero. To reduce artifacts from discontinuous data, a 1/4-second half-Hann-window ramping from unity to zero was multiplied against the data stream prior to each zeroed interval, and a 1/4-second half-Hann window ramping from zero back to unity was multiplied at the end of zeroed intervals. This gating can be considered to be inverse-Tukey-windowed. Although the Tukey windowing mitigates severe spectral artifacts, the resulting spectra still suffer visible spectral leakage very near loud instrumental lines, such as from 60-Hz power mains and "violin modes" (near 500 Hz) due to ambient vibrations of the silica fibers from which LIGO mirrors are suspended. All gated intervals longer than 30 seconds are excluded from analysis, as are 7200s SFTs containing total gate durations longer than 120 seconds. Altogether, the applied gating leads in this analysis to losses of about 1% and 11% of the H1 and L1 observation times during the O3a epoch for search frequencies below 475 Hz. Details of the gating, including validation that low-frequency CW "hardware injections" (simulated signals imposed on interferometer mirrors during data taking, see Sec. III E) are recovered with higher signal-to-noise ratio (SNR) in gated data than in the original, ungated data can be found in a technical report [32].

As discussed in Sec. III, the PowerFlux program searches many narrow frequency bands, where the SFT coherence time chosen depends on frequency. In general, longer coherence times give improved sensitivity, but incur larger computational costs from the need to search more finely in parameter space. In addition, efficiency loss from spectral

TABLE I. Information on the short Fourier transforms (SFTs) used in the search. All SFTs are Hann-windowed with 50% overlap. The numbers of gated SFTs used below 475 Hz are affected by live time loss from avoiding data stretches with high rates of gated glitches, with a larger effect seen for L1 data.

	20–475 Hz	475–1475 Hz	1475–2000 Hz
Dataset	Gated C01	Ungated C01	Ungated C01
Coherence time	7200s	3600s	1800s
Number of SFTs	H1: 2287 L1: 2247	H1: 5535 L1: 5973	H1: 11735 L1: 12574

leakage due to Doppler modulations from the Earth's motion increases at higher frequency, especially for sources near the ecliptic plane. Given these tradeoffs, the same coherence-time choices made for the O1 analysis [8] are chosen here, as shown in Table I. The SFTs are created from the C01 calibrated strain data [34], using Hann windowing and 50% overlap. Upper limits on the calibration uncertainties over the 20–2000 Hz band in the O3a epoch are estimated to be <7% in magnitude and <4 deg in phase (68% confidence interval).

III. ANALYSIS METHOD

This search uses the PowerFlux program [3,5,7,8] with loose-coherence follow-up of outliers [9,10]. In brief, strain power is summed over many SFTs after correcting for Doppler modulations, for a large bank of templates based on sky location, frequency, frequency derivative and stellar orientation. The maximum strain powers detected over the entire sky and for all frequency derivatives in each narrow frequency subband (see Table II for the frequency-dependent widths) define strict frequentist upper limits. Initial outliers, defined by high values of SNR, are followed up in a multistage search with increasing levels of effective coherence at each stage to increase the expected SNR for true signals. Candidates passing all stages are examined individually to determine their credibility as gravitational wave sources, with further warranted follow-up carried out in the full O3 dataset.

A. Signal model and parameter space searched

The signal templates assume a classical model of a spinning neutron star with a time-varying quadrupole moment that produces circularly polarized gravitational radiation along the rotation axis, linearly polarized radiation in the directions perpendicular to the rotation axis and elliptical polarization for the general case. The star's orientation, which determines the polarization, is parametrized by the inclination angle ι of its spin axis relative to the detector line-of-sight and by the angle ψ of the axis projection on the plane of the sky. The linear polarization case ($\iota = \pi/2$) is the most unfavorable because the gravitational wave flux impinging on the detectors is smallest for an intrinsic strain amplitude h_0, possessing 8 times less incident strain power than for circularly polarized waves ($\iota = 0, \pi$).

The strain signal model $h(t)$ for a periodic source is assumed to be the following function of time t:

$$h(t) = h_0\left(F_+(t,\alpha_0,\delta_0,\psi)\frac{1+\cos^2(\iota)}{2}\cos(\Phi(t)) + F_\times(t,\alpha_0,\delta_0,\psi)\cos(\iota)\sin(\Phi(t))\right), \quad (1)$$

where h_0 is the intrinsic strain amplitude, $\Phi(t)$ is the signal phase, F_+ and $F_\times$ characterize the detector responses to signals with "+" and "×" quadrupolar polarizations [3], and the sky location is described by right ascension α_0 and declination δ_0.

In a rotating triaxial ellipsoid model for a star at distance r spinning at frequency $f_{\rm rot}$ about its (approximate) symmetry axis (z), the amplitude h_0 can be expressed as

$$h_0 = \frac{4\pi^2 G\epsilon I_{zz} f_{\rm GW}^2}{c^4 r} \quad (2)$$

$$= [1.1\times10^{-24}]\left[\frac{\epsilon}{10^{-6}}\right]\left[\frac{I_{zz}}{I_0}\right]\left[\frac{f_{\rm GW}}{1\ \rm kHz}\right]^2\left[\frac{1\ \rm kpc}{r}\right], \quad (3)$$

where $I_0 = 10^{38}\ \rm kg\cdot m^2$ ($10^{45}\ \rm g\cdot cm^2$) is a nominal neutron star moment of inertia I_{zz} about z, and the gravitational radiation is emitted at frequency $f_{\rm GW} = 2f_{\rm rot}$.

TABLE II. Information on the band-specific parameters for the initial search (stage 0) and outlier follow-up stages. The number of spin-down steps and the spin-down step size refer to the templates used in the stage-0 search. The tolerances refer to the consistency requirements between H1 and L1 outliers used to define candidates selected for stage-1 follow-up. Other search parameters relevant to all search bands are described in the text.

	20–475 Hz	475–1475 Hz	1475–2000 Hz
Frequency bin width	0.139 mHz	0.278 mHz	0.556 mHz
Number of spin-down templates	66	34	18
Spin-down step size (Hz/s)	1.692×10^{-10}	3.333×10^{-10}	6.667×10^{-10}
H1/L1 frequency mismatch tolerance (mHz)	2.5	2.5	2.5
H1/L1 spin-down mismatch tolerance (Hz/s)	3.0×10^{-10}	3.0×10^{-10}	3.0×10^{-10}

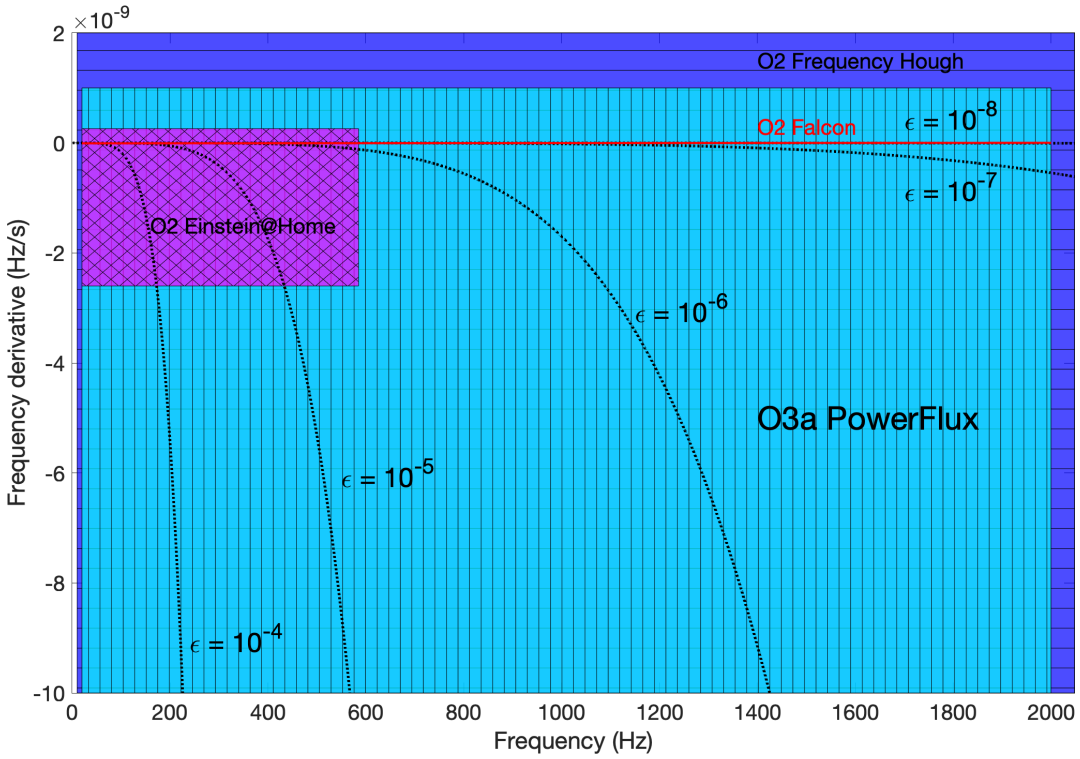

FIG. 1. Comparison in frequency and spin-down for this search with those of previous all-sky searches of LIGO O2 data. The shaded rectangle with vertical bars shows the 20–2000 Hz and -10^{-8}–10^{-9} Hz/s range for this O3a search. The slightly larger rectangle with horizontal bars shows the region searched in the O2 data with the Frequency Hough method [12,13]. The smaller rectangle with crossed diagonal bars shows the region searched by the distributed-computing project Einstein@Home [14]. The solid line at zero spin-down depicts the specialized O2 search for low-ellipticity millisecond pulsars using the Falcon method [15–17] (the thickness of the line overstates the coverage in spin-down range). The dotted curves indicate contours of constant equatorial ellipticity $\epsilon = (10^{-8}, 10^{-7}, 10^{-6}, 10^{-5}$ and $10^{-4})$ for a star with stellar spin-down dominated by gravitational wave emission.

The equatorial ellipticity ϵ is a convenient, dimensionless measure of stellar nonaxisymmetry,

$$\epsilon \equiv \frac{I_{xx} - I_{yy}}{I_{zz}}. \tag{4}$$

The phase evolution of the signal is given in the reference frame of the Solar System barycenter (SSB) by the second-order approximation,

$$\Phi(t) = 2\pi(f_{\text{source}} \cdot (t - t_0) + f^{(1)} \cdot (t - t_0)^2/2) + \phi, \tag{5}$$

where f_{source} is the SSB source frequency, $f^{(1)}$ is the first frequency derivative (which, when negative, is termed the spin-down), t is the SSB time, and the initial phase ϕ is computed relative to reference time t_0. When expressed as a function of the local time of ground-based detectors, Eq. (5) acquires sky-position-dependent Doppler shift terms.

We search a frequency band 20–2000 Hz and a frequency derivative $\dot{f}$ range of $[-1 \times 10^{-8}, +1 \times 10^{-9}]$ Hz s^{-1}. Figure 1 shows this parameter space coverage together with those of previous all-sky searches of the LIGO O2 data using different methods. Most natural sources are expected to have a negative first frequency derivative, as the energy lost in gravitational or electromagnetic waves would make the source spin more slowly. A small number of isolated pulsars in globular clusters exhibit slight apparent spin-up, believed to arise from acceleration in the Earth's direction; known apparent spin-up values have magnitudes too small to prevent source detection with the zero-spin-down templates used in this search, given a strong enough signal. The frequency derivative can also be positive when the source is affected by a strong slowly varying Doppler shift, such as due to a long-period orbit with a companion. A more exotic source of spin-up is gravitational wave superradiance from a boson cloud in the vicinity of an isolated black hole [35].

All known isolated pulsars spin down more slowly than the maximum value of $|\dot{f}|_{\text{max}}$ used here, and as seen in the results section, the equatorial ellipticity required for higher $|\dot{f}|$ is improbably high for a source losing rotational energy primarily via gravitational radiation at low frequencies. More plausible is a source with spin-down dominated by electromagnetic radiation energy loss, but for which detectable gravitational radiation is also emitted.

One measure of gravitational wave detectability of known pulsars is the "spin-down strain limit" defined by equating inferred rotational kinetic energy loss to gravitational wave energy emission. For the frequency band searched here, such limits range from as high as $O(10^{-24})$ for energetic, low-frequency young stars, such as the Crab and Vela pulsars, down to below 10^{-27} for high-frequency millisecond pulsars [36], where the highest such limit at high frequencies is $O(10^{-26})$.

B. Methodology

The PowerFlux pipeline has a hierarchical structure that permits systematic follow-up of loud outliers from the initial stage. The later stages improve intrinsic strain sensitivity by increasing effective coherence time while dramatically reducing the parameter space volume over which the follow-up is pursued. The pipeline uses loose coherence [9] with stages of improving refinement via steadily increasing effective coherence times. Any outliers that survive all stages of the search pipeline are examined manually for contamination from known instrumental artifacts and for evidence of contamination from a previously unknown single-interferometer artifact. Those for which no artifacts are found are subjected to further follow-up described below.

In the pipeline's initial stage, the main PowerFlux algorithm [3–8] establishes upper limits and produces lists of outliers. The program sets strict frequentist upper limits on detected strain power in circular and linear polarizations that apply everywhere on the sky except for small regions near the ecliptic poles, where signals with small Doppler modulations can be masked by stationary instrumental spectral lines. The procedure defining these excluded regions is described in [5] and applies to less than 0.2% of the sky over the entire run, where the precise shapes of the regions near the poles depend on assumed signal frequency and spin-down. Initial outliers are defined by a joint H1-L1 signal-to-noise ratio (SNR) greater than a threshold of 7, with consistency among corresponding H1, L1 and joint H1-L1 outliers (criteria described in Sec. III D). These outliers are then followed up with a loose-coherence detection pipeline [5,9,10], which is used to reject or confirm the outliers.

The power calculation of the data can be expressed as a bilinear form of the input matrix $\{a_{t,f}\}$ constructed from the SFT coefficients with indices representing time and frequency,

$$P[f] = \sum_{t_1,t_2,D_i,D_j} a^{(D_i)}_{t_1,f+\Delta f(t_1)} a^{(D_j)*}_{t_2,f+\Delta f(t_2)} K^{D_iD_j}_{t_1,t_2,f}. \quad (6)$$

In this expression $\Delta f(t)$ is the detector-frame frequency drift due to the effects from both Doppler shifts and the first frequency derivative. The sum is taken over all times t corresponding to the midpoints of the SFT time intervals. The kernel $K^{(D_iD_j)}_{t_1,t_2,f}$ includes the contribution of time-dependent SFT noise weights, antenna response, signal polarization parameters, and relative phase terms [9,10] for detectors $D_{i,j}(=\mathrm{H1},\mathrm{L1})$. Separate power sums are computed for H1, L1 and combined H1-L1 data.

TABLE III. PowerFlux outlier follow-up parameters. Stage 1 and higher use a loose-coherence algorithm for demodulation. The sky (both right ascension α and declination δ_0) and frequency refinement parameters are relative to values used in the stage 0 PowerFlux search.

Stage	Instrument sum	Phase coherence δ rad	Spin-down step Hz/s	Sky refinement $\alpha \times \delta_0$	Frequency refinement	SNR increase %
		20–60 Hz frequency range, 7200 s SFTs, 0.0625 Hz frequency bands				
0	Initial/upper limit incoherent	NA	1.692×10^{-10}	1	1/2	···
1	Incoherent	$\pi/2$	1.0×10^{-10}	$1/4 \times 1/4$	1/8	20
2	Coherent	$\pi/2$	5.0×10^{-11}	$1/4 \times 1/4$	1/8	10
		60–475 Hz frequency range, 7200 s SFTs, 0.0625 Hz frequency bands				
0	Initial/upper limit incoherent	NA	1.692×10^{-10}	1	1/2	···
1	Incoherent	$\pi/2$	1.692×10^{-10}	$1/4 \times 1/4$	1/8	20
2	Coherent	$\pi/2$	5.0×10^{-11}	$1/4 \times 1/4$	1/8	10
		475–1475 Hz frequency range, 3600 s SFTs, 0.125 Hz frequency bands				
0	Initial/upper limit incoherent	NA	3.33×10^{-10}	1	1/2	···
1	Incoherent	$\pi/2$	3.33×10^{-10}	$1/4 \times 1/4$	1/8	15
2	Coherent	$\pi/2$	5.0×10^{-11}	$1/4 \times 1/4$	1/8	10
		1475–2000 Hz frequency range, 1800 s SFTs, 0.25 Hz frequency bands				
0	Initial/upper limit incoherent	NA	6.67×10^{-10}	1	1/2	···
1	Incoherent	$\pi/2$	3.33×10^{-10}	$1/4 \times 1/4$	1/8	15
2	Coherent	$\pi/2$	5.0×10^{-11}	$1/4 \times 1/4$	1/8	10

The fast first-stage (stage 0) PowerFlux algorithm uses a kernel with diagonal terms only (including separate single-detector contributions $D_i = D_j$). The second stage (stage 1) increases effective coherence time while still allowing for controlled deviation in phase [9] via kernels that increase effective coherence length by inclusion of limited single-detector, off diagonal terms. The third stage (stage 2) maintains the stage-1 effective coherence time, but adds SFT coefficients from H1 and L1 data coherently ($D_i \neq D_j$) to improve SNR and parameter resolution.

The effective coherence length is captured in a parameter δ [9], which describes the degree of phase drift allowed between SFTs. A value of $\delta = 0$ corresponds to a fully coherent case, and $\delta = \pi$ corresponds to incoherent power sums.

Depending on the terms used, the data from different interferometers can be combined incoherently (such as in stages 0 and 1, see Table III) or coherently (as used in stage 2). The coherent combination is more computationally expensive but improves parameter estimation.

C. Upper limits determination

The 95% confidence-level (C.L.) upper limits presented in Sec. IV are reported in terms of the worst-case value of h_0 (linear polarization) and for the most sensitive case of circular polarization.

These upper limits, produced in stage 0, are based on the overall noise level and largest outlier in strain found for every template in each narrow subband in the first stage of the pipeline. Subbands are analyzed by separate instances of PowerFlux [5].

To allow robust analysis of the entire spectrum, including regions with severe spectral artifacts, a *universal statistic* algorithm [7,37] is used for establishing upper limits. The algorithm is derived from the Markov inequality and shares its independence from the underlying noise distribution. It produces upper limits less than 5% above optimal in case of Gaussian noise. In non-Gaussian bands, it can report values larger than what would be obtained if the true underlying distribution were known, but the upper limits are always at least 95% valid. Figure 2 shows results of a high-statistics "software injections" simulation run performed as described in [5]. Correctly established upper limits lie above the dashed diagonal lines (defining equality between upper limit obtained and true injection strain) in each panel, corresponding to four selected subbands [SFT coherence times]: 20–60 Hz [7200s], 60–475 Hz [7200s], 475–1475 Hz [3600s] and 1475–2000 Hz [1800s]. Performance for the 7200s-SFT

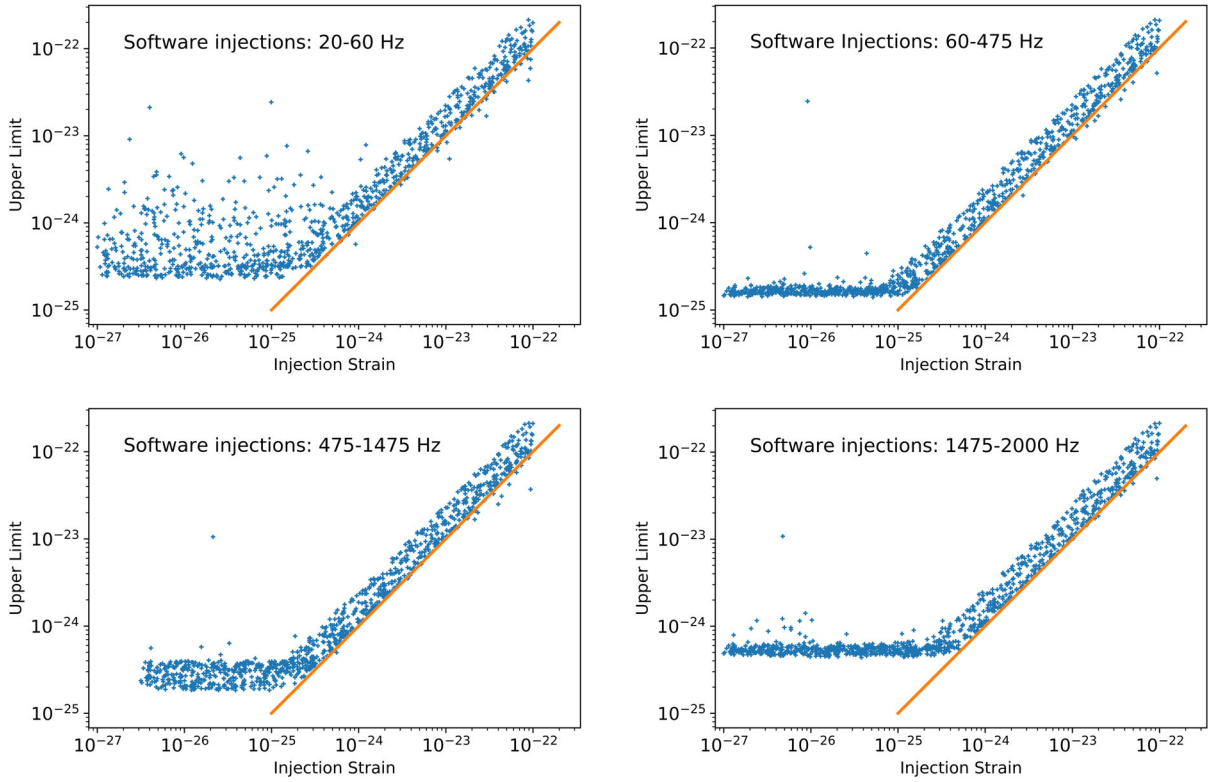

FIG. 2. Illustration of PowerFlux upper limit validation for very low, low, mid and high frequencies. Each point in the upper left, upper right, lower left and lower right panels represents a separate injection in the 20–60 Hz, 60–475 Hz, 475–1475 Hz and 1475–2000 Hz frequency ranges, respectively. Each established upper limit (vertical axis) is compared against the injected strain value defined by the horizontal axis (diagonal line defines equality of upper limit obtained and true injected strain). These injections are for random polarizations. Corresponding scatter plots for linearly polarized injections confirm the desired 95% coverage, regardless of polarization.

20–60 Hz and 60–475 Hz bands are shown separately because of the proliferation of spectral line artifacts below 60 Hz, primarily in the H1 data. The breakpoint frequencies of 475 Hz and 1475 Hz for decreasing SFT coherence time (Table I) are those used in the O1 PowerFlux search [7,8], marking the starts of bands disturbed by first and third violin mode harmonics. Additional band-specific parameters for the initial stage of the search are listed in Table II.

D. Outlier follow-up

A follow-up search for detection is carried out for high-SNR outliers found in stage 0. The outliers are subject to an initial coincidence test. For each outlier with SNR > 7 in the combined H1 and L1 data, we require there to be outliers in the individual detector data of the same small sky patch, approximately square with a side length ~ 30 mrad $\times$ (100 Hz/frequency) that have SNR > 5 and match the parameters of the combined-detector outlier within 2.5 mHz in frequency and 3×10^{-10} Hz/s in spin-down. The combined-detector SNR is additionally required to be above both single-detector SNRs, in order to suppress single-detector instrumental artifacts, except for unusually loud outliers (combined, H1 and L1 SNRs all greater than 20).

The identified outliers using combined data are then passed to the follow-up stage using a loose-coherence algorithm [9] with progressively improved determination of frequency, spin-down, and sky location.

As the initial stage 0 sums only powers, it does not use the relative phase between interferometers, which results in some degeneracy among sky position, frequency, and spin-down. The first loose-coherence follow-up stage (1) demands greater temporal coherence (smaller δ) within each interferometer, which should boost the SNR of viable outliers, but combines H1 and L1 power sums incoherently, The subsequent stage (2) uses combined H1 and L1 data coherently, providing tighter bounds on outlier location.

Testing of the stages 0–2 pipeline is performed for frequency bands searched via software injections using

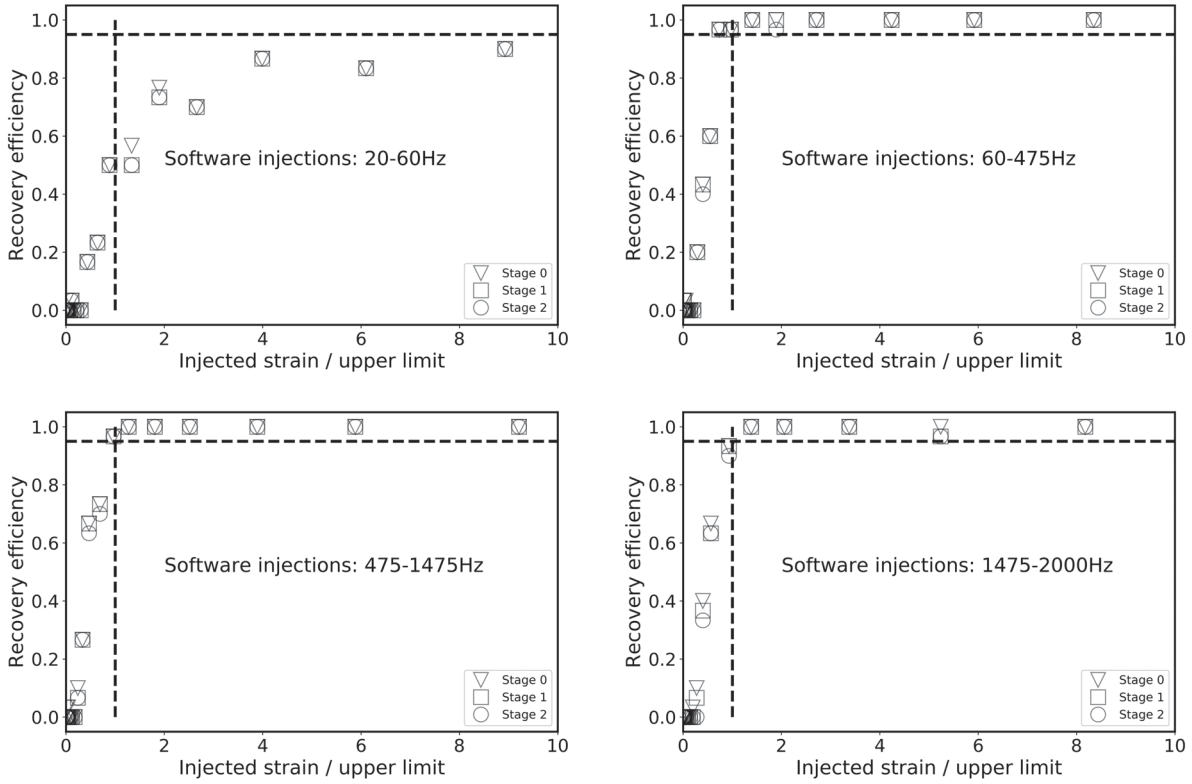

FIG. 3. Injection (software simulations) recovery efficiencies in the 20–60 Hz, 60–475 Hz, 475–1475 Hz and 1475–2000 Hz frequency bands are shown in the upper left, upper right, lower left and lower right panels, respectively, for stages 0, 1 and 2 of the search. The injected strain divided by the 95% C.L. upper limit in its band (without injection) is shown on the horizontal axis. The percentage of surviving injections is shown on the vertical axis, with a horizontal dashed line drawn at the 95% level. The vertical dashed line marks a relative strain of unity. Ideally, the recovery efficiencies should lie to the left of the vertical line or above the horizonal line. One observes, however, that the ideal recovery efficiency is significantly degraded below 60 Hz, where large instrumental artifacts in the H1 data and only modest expected Doppler modulations make clean signal recovery more challenging. Most of the degradation stems from the band below 27 Hz for which H1 line contamination is severe and for which the H1 noise floor is substantially higher than the L1 noise floor.

the same follow-up procedure. The recovery criteria also require that an outlier close to the true injection location (within 2.5 mHz in frequency f, 3×10^{-10} Hz/s in spin-down and 28.5 rad·Hz/f in sky location) be found and successfully pass through all stages of the detection pipeline.

Injection recovery efficiencies from simulations covering the major subbands (20–475 Hz, 475–1475 Hz, 1475–2000 Hz) are shown in Fig. 3 for stages 0, 1 and 2, which confirm that 95% signal recovery is comparable to the 95% upper limit in all bands, as desired, except for the region below 60 Hz for which spectral line artifacts heavily contaminate the H1 dataset. Injections in vetoed frequency bands (see Sec. IV B and Table VI) are not included in these graphs.

As in previous PowerFlux analyses with loose-coherence follow-up [7,8], only a mild influence from parameter mismatch is expected, as the parameters are chosen to accommodate the worst few percent of injections. The follow-up procedure establishes very wide margins for outlier follow-up. For example, when transitioning from the semicoherent stage 0 to the loose-coherence stage 1 below 475 Hz, the effective coherence length increases by a factor of 4. The average true signal SNR should then increase by more than 40%. But the threshold used in follow-up is only 15%–20%, depending on frequency, which accommodates unfavorable noise conditions, template mismatch, and detector artifacts.

Although a similar prior analysis [7,8] of O1 data used additional stages (3, 4) of loose coherence, we choose after stage 2 to inspect candidates manually. The small number not found to be contaminated by obvious instrumental artifacts are followed up in the full O3 dataset by a search similar to the PowerFlux O3a stage 1, but using much finer spin-down stepping of 1×10^{-11} Hz/s, and refinement factors of 1/4 for both sky (right ascension and declination each) and frequency stepping, to exploit the improved SNR and parameter resolution possible in the nearly doubled observation span. Any outlier surviving this full-O3 follow-up is explored via a more sensitive method, implemented in PyFstat [38,39] which uses Markov chain Monte Carlo (MCMC) techniques [40,41] to explore small regions of parameter space in successive stages of increasing coherence times.

The full-O3 PowerFlux follow-up search uses nearly 11 months of data (compared to the 6-month O3a period), leading to an expected increase in SNR by a factor of approximately $\sqrt{11/6} = 1.35$, with an additional ∼40% increase from the use of stage-1 loose coherence, leading to a nominal expectation of SNR gain of a factor of ∼1.9. Software simulations of signals with amplitudes as weak as 1/3 of the upper limit in a given band, however, reveal large fluctuations above and below this expectation for all search bands. These simulations suggest applying a conservative (negligible efficiency loss) threshold on the SNR increase of only 20%, which is nonetheless effective in suppressing most noise artifacts.

TABLE IV. Key parameters of the hardware-injected simulated isolated-source continuous wave signals during the O3 data run (epoch GPS 1238166018) with nominal frequencies between 20 and 2000 Hz, along with upper limits in the nominal signal bins and in the six nearest control bins. The last column states whether or not the injection is detected in outlier follow-up. Most of the injection amplitudes are significantly weaker than those used in prior observing runs, leading to fewer detections than in past analyses. The amplitudes quoted here are the *intended* values; uncertainties in the approximate actuation functions used in the online injection system may be as large as a few percent, depending on frequency. Also, a now-known error in the actuation function used for L1 injections led to an unintended time delay of approximately 122 μs, which corresponds to a phase lag in the highest-frequency injection (2991 Hz) of ∼130° and degrades coherent H1-L1 injection recovery.

Label	Frequency Hz	Spindown nHz/s	RA_{J2000} degrees	DEC_{J2000} degrees	h_0 true	UL sig bin	UL ctrl bins	Detected?
Inj0	265.575086	-4.15×10^{-3}	71.55193	−56.21749	6.12×10^{-26}	1.8×10^{-25}	1.8×10^{-25}	Yes
Inj1	848.937350	-3.00×10^{-1}	37.39385	−29.45246	5.47×10^{-25}	8.1×10^{-25}	3.6×10^{-25}	Yes
Inj2	575.163506	-1.37×10^{-4}	215.25617	3.44399	7.59×10^{-26}	2.7×10^{-25}	2.7×10^{-25}	No
Inj3	108.857159	-1.46×10^{-8}	178.37257	−33.4366	1.30×10^{-25}	1.9×10^{-25}	1.9×10^{-25}	No
Inj4	1390.806586	$-2.54 \times 10^{+1}$	279.98768	−12.4666	1.07×10^{-24}	4.9×10^{-25}	4.9×10^{-25}	Yes[a]
Inj5	52.808324	-4.03×10^{-9}	302.62664	−83.83914	3.99×10^{-25}	5.7×10^{-25}	3.2×10^{-25}	Yes
Inj6	145.444975	-6.73×10^{0}	358.75095	−65.42262	3.84×10^{-25}	4.3×10^{-25}	2.2×10^{-25}	Yes
Inj7	1220.434717	-1.12×10^{0}	223.42562	−20.45063	1.65×10^{-25}	4.5×10^{-25}	4.4×10^{-25}	No
Inj8	190.100215	-8.65×10^{0}	351.38958	−33.41852	1.30×10^{-25}	1.8×10^{-25}	1.7×10^{-25}	Yes
Inj9	763.847316	-1.45×10^{-8}	198.88558	75.68959	1.30×10^{-25}	3.1×10^{-25}	3.0×10^{-25}	No
Inj10	26.332768	-8.50×10^{-2}	221.55565	42.87730	6.26×10^{-25}	1.9×10^{-24}	1.2×10^{-24}	No
Inj11	31.424704	-5.07×10^{-4}	285.09733	−58.27209	3.17×10^{-25}	9.4×10^{-25}	7.8×10^{-25}	No
Inj12	37.805210	-6.25×10^{0}	331.85267	−16.97288	2.63×10^{-25}	4.8×10^{-25}	4.9×10^{-25}	No
Inj14	1991.092292	-1.00×10^{-3}	300.80284	−14.32394	1.83×10^{-24}	2.1×10^{-24}	8.1×10^{-25}	Yes

[a]True spin-down value outside of nominal search range. Injection is recovered when search range is extended for this band.

The final follow-up method applied to any survivors of the full-O3 loose-coherence check uses the PYTHON-based PYFstat [38,39] software infrastructure to combine a MCMC approach [40,41] with semicoherent summing of the well known $\mathcal{F}$-statistic detection statistic [42]. In this approach, the parameter space near to those values from a stage-2 outlier is sampled randomly according to a certain probability density function determined by the $\mathcal{F}$-statistic likelihood function. We closely follow an implementation [41] applied to a recent analysis of O2 data to follow up on outliers emerging from several prior O2 continuous wave searches.

Briefly, the O3a observation time is divided into N_{seg} segments, for each of which the $\mathcal{F}$-statistic is computed over a coherence time approximately equal to the observation time divided by N_{seg}. For each point sampled in parameter space, the sum of the $\mathcal{F}$-statistic values is computed to form a total detection statistic. This procedure is repeated, decreasing the number of segments (increasing the coherence time), using the resulting MCMC-maximized $\mathcal{F}$-statistic sum as the seed for the next stage, with a consequent reduction in parameter space volume searched. For this O3a analysis we choose five successive stages of follow-up with decreasing values of $N_{\mathrm{seg}} = 500$ (coherence time of 0.36 day), 250, 55, 5 and 1. A random sample of 600 off-source sky locations having the same declination as the putative signal direction, but separated by more than 90 deg from that direction, is used to determine a nonsignal expectation for the background distributions in the same frequency band [41]. A Bayes factor B_{SN} is computed from the change in $\mathcal{F}$-statistic values for a nominal signal compared to the empirical background distribution in the last stage ($N_{\mathrm{seg}} = 5$ to $N_{\mathrm{seg}} = 1$).

E. Hardware injections

During the O3 run 18 hardware injections were used to simulate particular CW signals, as part of detector response validation, including long-term phase fidelity. The injections were imposed via radiation pressure from auxiliary lasers [43]. For reference, Table IV lists the key source parameters for the 14 injections relevant to this analysis (labeled Inj0-Inj12 and Inj14), namely those that simulate isolated neutron stars with nominal frequencies between 20 and 2000 Hz. In general, the injection amplitudes used in

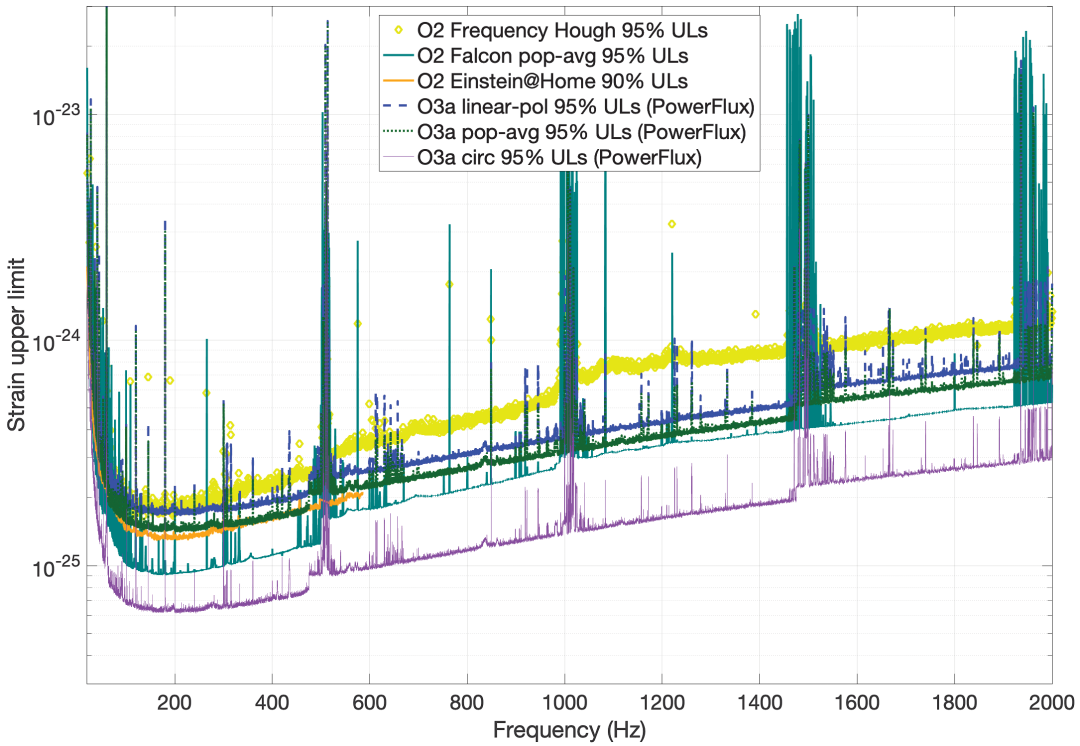

FIG. 4. Upper limits on gravitational strain amplitude for this O3a analysis and for previous O2 analyses. The dark blue curve shows worst-case (linearly polarized) 95% CL upper limits in analyzed (62.5 mHz, 125 mHz, 250 mHz) sub-bands for the broad (20–475 Hz, 475–1475 Hz, 1475–2000 Hz) search bands. The lowest, purple curve shows upper limits assuming a circularly polarized source. The middle (green) curve shows approximate population-averaged all-sky upper limits inferred from the circularly polarized limits. For comparison, the uppermost yellow-green diamonds show previous population-averaged 95% CL all-sky upper limits derived from LIGO O2 data using the Frequency Hough method [12,13]. The orange curve shows 90% CL upper limits from the O2 Einstein@Home search [14] over the band 20–585.15 Hz and over a spin-down range that is 26% of the range used here. The light blue curve shows 95% CL upper limits from the O2 Falcon search [15–17] over the 20–2000 Hz band and a severely restricted spin-down range. See Fig. 1 for a comparison of parameter space coverage from these various searchers.

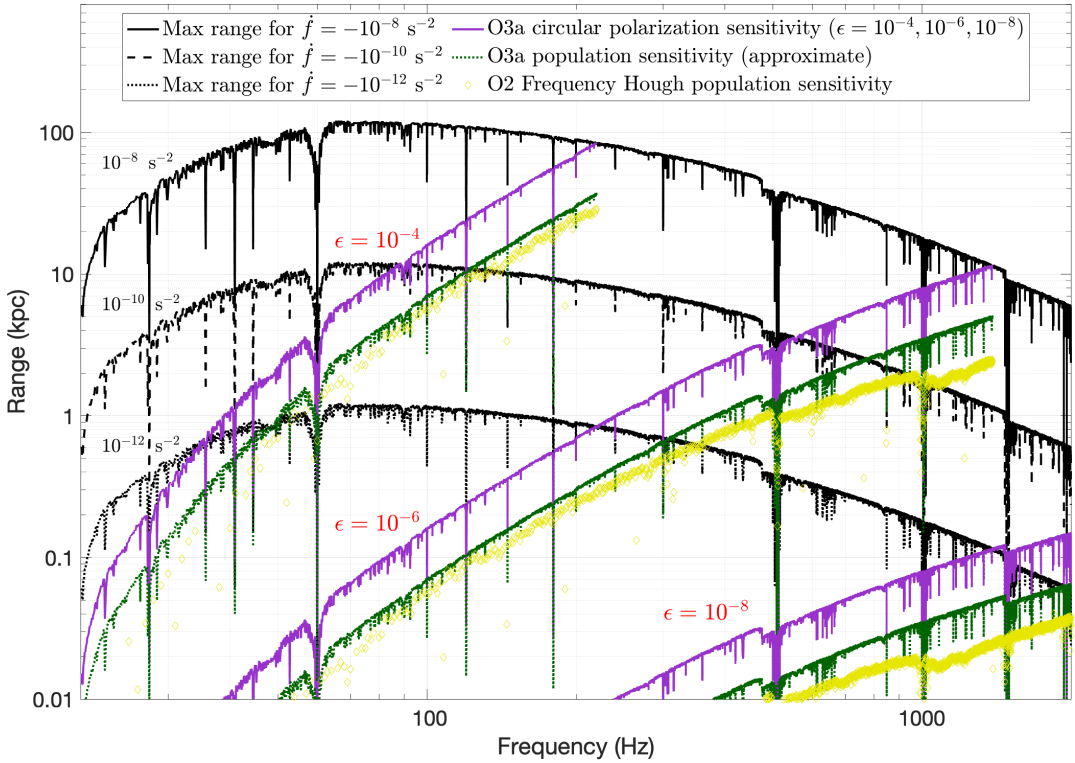

FIG. 5. Ranges (kpc) of the PowerFlux search for neutron stars spinning down solely due to gravitational radiation ("gravitars") under different assumptions. The three sets of three curves (purple, green dotted, yellow-green diamonds) that generally rise with frequency are the ranges for which the O3a circular-polarization, O3a population-averaged and O2 population-averaged Frequency Hough [12,13] upper limits apply for three different assumed equatorial ellipticities of $\epsilon = 10^{-4}$, 10^{-6} and 10^{-8}. In each case, the curve stops at the frequency at which the implied spindown magnitude at the corresponding range exceeds the maximum range allowed by the maximum spindown magnitude (10^{-8} Hz/s) used in these analyses. The three black curves (solid, dashed, dot-dashed) that peak below 100 Hz represent the maximum possible ranges for which the O3a circular-polarization limits apply under the assumption that the maximum spindown magnitude is $(10^{-8}, 10^{-10}, 10^{-12})$ Hz/s. Searching for high spindown magnitudes simultaneously probes higher ellipticities and larger regions of the galaxy, reaching well beyond the galactic center (~8.5 kpc) at high ellipticities and low frequencies. More realistically, a neutron star's spin-down may be dominated by electromagnetic radiation, in which case searching for high spindown magnitude achieves a shorter search range, but enables detection of stars that would not be detected under the gravitar assumption. (color online).

TABLE V. Counts of outliers surviving different stages of the hierarchical follow-up for four frequency bands. Survivors from stage-2 follow-up are broken down into the categories of hardware injections, visible artifacts identified via strain histograms and candidates for loose-coherence follow-up in the full-O3 data. Only one cluster of O3a outliers (near 1663.6 Hz) survives the full-O3 fine-grained follow-up, leading to a cluster of 21 full-O3 outliers. Additional follow-up of these weak candidates, which appear in a visibly disturbed band of L1 data, was carried out using the MCMC PyFstat follow-up procedure described in section III D. The PyFstat follow-up confirmed these 21 outliers to be uninteresting.

	20–60 Hz	60–475 Hz	475–1475 Hz	1475–2000 Hz
Stage 0	988	54500	65746	21883
Stage 1	2804	3259	24046	2494
Stage 2	3640	21296	506	5973
HW injections	3440	15294	448	4957
Visible artifacts	199	5997	48	996
Full-O3 follow-up	1	5	10	20
Full-O3 survivors	0	0	0	21

the O3 run are substantially lower than those used in previous observing runs. For this reason, some injections with identical source parameters, except for stronger signal amplitudes, were detected with high SNR in the O2 run, but are not detected in this analysis, although they can be found with targeted matched-filter analyses.

For each injection in Table IV, the column labeled "UL sig bin" gives the 95% UL (upper limit) for the corresponding band. Ideally, that value should exceed the true injected amplitude h_0 for at least 95% of the injections. In this case, that statement holds for all 14 injections. The column labeled "UL ctrl bins" shows the average 95% UL for the six nearest neighboring frequency subbands as a rough guide to the expected value in the absence of an injection (or true signal).

The last column states whether or not the injection survives all stages of loose-coherence follow-up. As hoped, all five injections with a true h_0 amplitude above the expected background estimation of the UL do survive these follow-up stages, as do two additional injections with somewhat smaller amplitudes.

IV. SEARCH RESULTS

Carrying out the stage-0 analysis described above leads to a set of all-sky upper limits (95% C.L.) on strain

TABLE VI. Frequency bands vetoed from outlier follow-up because of excessive outlier counts from instrumental artifacts. The stage at which outlier followup is aborted is also shown for each band. Altogether, about 257 Hz out of the 1980-Hz original search band was vetoed, or about 13%. Figure 6 shows these vetoed bands graphically.

$f_{\mathrm{low}}^{\mathrm{veto}}$ (Hz)	$f_{\mathrm{high}}^{\mathrm{veto}}$ (Hz)	Δf^{veto} (Hz)	Stage applied	$f_{\mathrm{low}}^{\mathrm{veto}}$ (Hz)	$f_{\mathrm{high}}^{\mathrm{veto}}$ (Hz)	Δf^{veto} (Hz)	Stage applied	$f_{\mathrm{low}}^{\mathrm{veto}}$ (Hz)	$f_{\mathrm{high}}^{\mathrm{veto}}$ (Hz)	Δf^{veto} (Hz)	Stage applied
25.462	25.788	0.325	2	656.994	657.446	0.451	1	1491.201	1501.600	10.399	0
33.045	33.355	0.311	2	663.264	663.716	0.453	1	1502.660	1503.410	0.751	0
35.539	35.876	0.336	2	666.423	666.877	0.453	1	1503.800	1504.700	0.901	0
38.266	38.614	0.348	2	669.273	669.727	0.454	1	1510.119	1513.071	2.952	0
38.666	39.084	0.418	2	898.520	899.510	0.990	1	1516.948	1520.162	3.214	0
39.256	39.664	0.408	2	899.740	900.240	0.500	1	1527.817	1528.773	0.956	0
40.696	41.164	0.468	2	906.559	907.081	0.521	1	1531.547	1532.183	0.636	0
49.835	50.165	0.330	2	909.839	910.361	0.522	1	1533.507	1535.263	1.757	0
299.200	299.980	0.780	2	918.518	919.082	0.564	1	1537.976	1538.614	0.638	0
301.870	302.530	0.660	2	922.408	922.922	0.515	1	1539.536	1540.494	0.958	0
302.960	303.630	0.671	2	944.586	948.745	4.159	1	1543.856	1545.675	1.819	0
305.819	306.581	0.761	2	946.735	947.235	0.499	1	1549.535	1552.165	2.630	0
307.149	307.881	0.732	2	947.535	948.035	0.500	1	1652.784	1653.416	0.633	2
314.619	315.482	0.863	2	948.235	948.735	0.500	1	1664.514	1665.186	0.673	2
399.800	400.190	0.390	0	958.774	959.276	0.502	1	1666.303	1667.037	0.733	2
409.409	411.191	1.782	0	959.744	960.256	0.512	1	1891.191	1891.909	0.718	1
432.807	436.994	4.187	0	960.744	961.256	0.512	1	1891.961	1892.669	0.708	1
487.001	489.599	2.598	2	962.634	963.136	0.503	1	1922.858	1924.262	1.405	1
492.301	517.002	24.701	2	963.134	963.636	0.503	1	1927.857	1929.463	1.606	1
519.298	531.303	12.005	2	963.834	964.336	0.503	1	1930.237	1930.953	0.716	1
598.740	600.220	1.480	1	964.334	966.337	2.003	1	1930.957	1932.793	1.836	1
604.220	604.760	0.541	1	977.752	1051.855	74.103	0	1935.156	1937.844	2.687	1
606.349	606.971	0.621	1	1082.832	1083.368	0.537	2	1939.256	1940.044	0.788	1
611.889	612.811	0.922	1	1083.432	1083.968	0.537	2	1939.906	1941.354	1.448	1
614.519	615.312	0.793	1	1099.720	1100.250	0.530	2	1944.456	1945.194	0.739	1
629.147	630.663	1.516	1	1152.825	1153.375	0.551	2	1944.705	1945.415	0.709	1
633.087	633.543	0.457	1	1197.970	1199.710	1.740	0	1949.955	1963.556	13.601	1
634.127	634.573	0.447	1	1199.710	1200.260	0.550	0	1965.453	1969.847	4.394	1
638.136	638.574	0.438	1	1208.779	1209.921	1.142	0	1974.253	1975.518	1.265	1
638.436	638.884	0.448	1	1213.179	1214.331	1.153	0	1976.582	1977.418	0.835	1
640.266	640.714	0.448	1	1224.797	1225.943	1.145	0	1977.802	1979.238	1.436	1
642.426	642.864	0.439	1	1229.997	1230.943	0.946	2	1980.342	1981.088	0.746	1
641.976	642.424	0.448	1	1259.424	1261.776	2.352	0	1984.901	1986.019	1.117	1
647.975	648.425	0.450	1	1333.007	1333.653	0.647	2	1988.091	1989.519	1.428	1
648.275	648.725	0.450	1	1458.704	1474.297	15.593	2	1995.815	1996.519	0.703	1
650.935	651.385	0.450	1	1478.752	1479.548	0.796	0	1999.590	2000.350	0.760	1
652.585	653.035	0.451	1	1480.702	1483.498	2.796	0				
655.954	657.406	1.451	1	1488.961	1489.699	0.738	0				

amplitude for worst-case, linear polarization (relative stellar spin orientation) and for best-case, circular polarization. That analysis also leads to an initial set of outliers for follow-up with later analysis stages. Whether or not a particular narrow frequency band contains an outlier, the upper limits obtained remain valid. As shown in Table IV, hardware injections were reliably recovered when their injected strain was at least 0.7 times the recorded upper

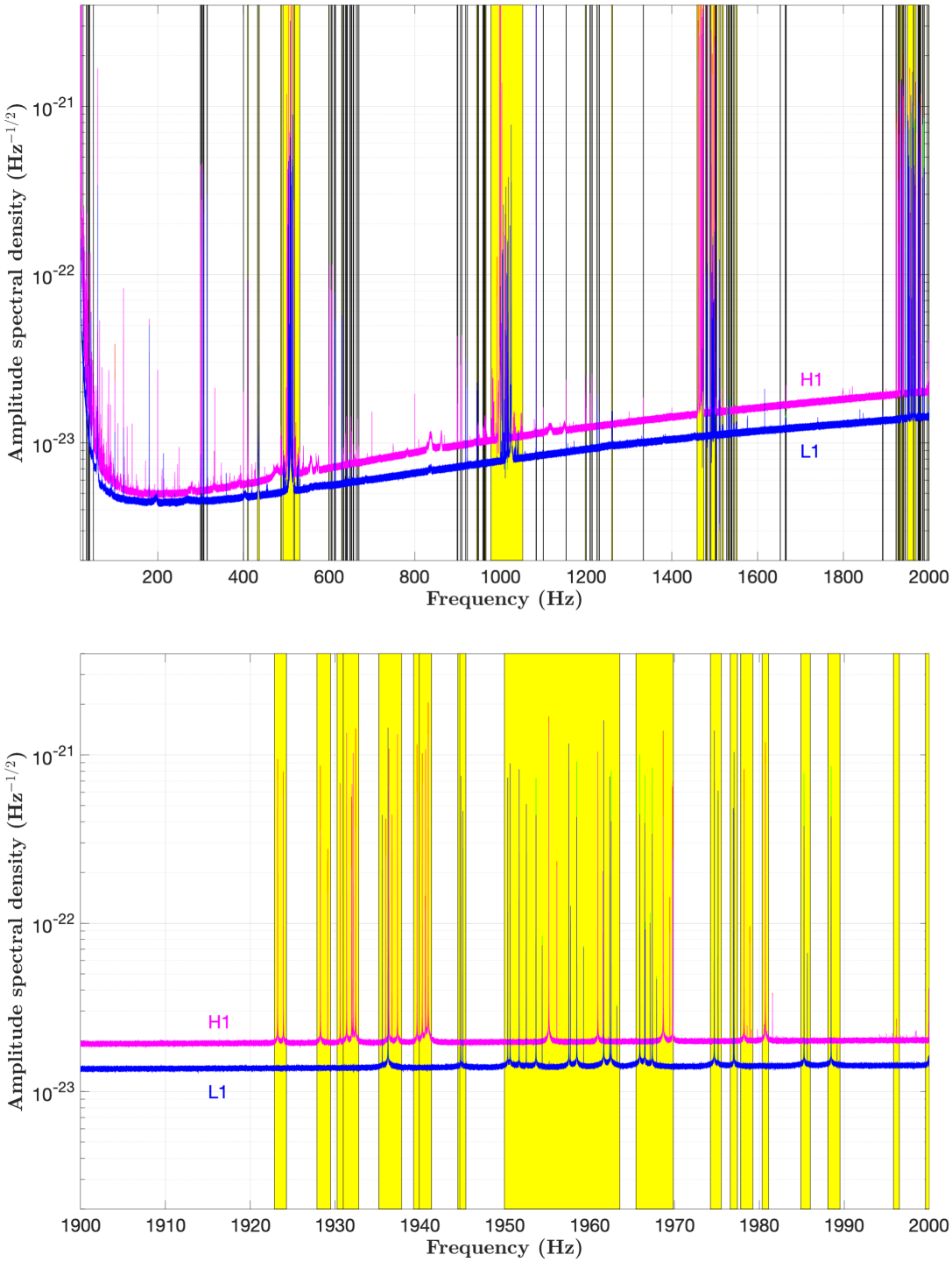

FIG. 6. Shaded regions (yellow) overlaid on the run-averaged spectra (inverse-noise weighted) from the H1 (magenta) and L1 (blue) O3a datasets indicate vetoed bands for which outlier follow-up is impeded by artifacts. The widest affected bands correspond to test-mass "violin modes" (ambient vibrations of the silica fibers from which LIGO mirrors are suspended) near multiples of 500 Hz. *Top panel:* Full 20–2000 Hz band. *Bottom panel:* Magnification of example 1900–2000 Hz band, for which line artifacts are dominated by the 4th harmonics of violin modes. (color online).

limit (and in one case as low as 0.34 times the upper limit). The upper limits obtained from stage-0 analysis are presented in section IV A, along with corresponding astrophysical sensitivities. Section IV B presents the results of outlier follow-up.

A. Upper limits and sensitivity

Figure 4 shows the upper limits obtained in this search as three curves, along with results from other all-sky searches in the O2 dataset [12–17]. The upper (blue) curve shows the upper limits for a worst-case (linear) polarization. The lowest (red) curve shows upper limits for an optimally oriented source (circular polarization). Both curves represent strict frequentist upper limits on these worst-case and best-case orientations with respect to location on the sky, spin-down and frequency within each narrow search band. For sensitivity comparisons with the previous O2 results, the intermediate (green) curve represents approximate population-averaged upper limits (over random sky locations and polarizations) and is derived from the circular polarization curve with a simple scale factor (2.3), based on injection studies in test bands.

Each linear-polarization or circular-polarization point in Fig. 4 represents a maximum over the sky, except for a small excluded portion of the sky near the ecliptic poles, which is highly susceptible to detector artifacts due to stationary frequency evolution produced by the combination of frequency derivative and Doppler shifts [5].

The O3a results presented here improve upon the previous O2 results in strain sensitivity with factors ranging from ∼1.2 at signal frequencies of ∼100 Hz to ∼2.0 at higher frequencies below the 1475-Hz breakpoint. The improvements at high frequencies come in part from the improved detector noise achieved with quantum squeezing [19] and in part from using longer Fourier transform coherence times than were used in the similar O2 analyses. At frequencies below ∼40 Hz, the O2 data was badly contaminated by instrumental lines [30], leading to poorer upper limits, and in some bands, precluding reliable upper limits using the method of [13]. The dramatically improved sensitivies obtained for low frequencies in this analysis come in part from mitigation of many spectral lines between the O2 and O3 runs, especially in the L1 interferometer, and in part from the use here of the "universal statistic" described in section III C.

One can recast these upper limits on source amplitude as lower limits on the range at which neutron stars with assumed equatorial ellipticity can reside. Figure 5 shows the ranges (kpc) of this search (circular-polarization and population-averaged) *vs.* frequency for assumed equatorial ellipticity values $\epsilon = 10^{-4}$, 10^{-6} and 10^{-8} and under the assumption that the *total* stellar spin-down magnitude does not exceed the 10^{-8} Hz/s maximum used in this search. The population-averaged ranges from prior O2 searches of comparable parameter space coverage [12,13] are also shown for these ellipticities. One sees a gain in range with respect to O2 analyses over the full frequency band, with the greatest improvements seen at highest frequencies, as expected. The number of accessible neutron stars is expected to rise at least quadratically as the range extends out into the plane of the galaxy and approaches the denser regions near its center, at a distance of ∼8.5 kpc, enhancing the detection probabilities from these range gains.

For reference, Fig. 5 also shows this search's implied maximum ranges *vs.* frequency for a "gravitar" (star with spin-down dominated by gravitational radiation) for maximum spin-down magnitudes of 10^{-8}, 10^{-10} and 10^{-12} Hz/s. If a neutron star's spin-down has major contributions from electromagnetic radiation, the range to which this search is sensitive for fixed ϵ may be reduced by the choice of maximum spin-down permitted. Conversely, searching for spin-down magnitudes much higher than expected for a gravitar of given ϵ could allow detection of a star with more realistic emission contributions.

TABLE VII. Parameters of the outliers surviving stage-2 follow-up, but discarded after visual inspection of a strain histogram confirmed instrumental contamination. Each outlier listed is the loudest after clustering in frequency, spin-down and sky location. Figure 7 shows a strain histogram example.

f (Hz)	df/dt (nHz/s)	R.A. (radians)	Dec. (radians)
32.5982	0.442	4.225	0.342
47.5005	−0.065	4.728	1.254
53.7245	−0.473	2.142	−1.107
54.3610	−1.639	4.497	−1.051
54.8529	−5.200	2.377	−1.338
64.3629	−6.569	5.266	−0.906
64.4101	0.250	0.457	1.232
70.0006	−0.100	1.543	−1.082
78.1135	0.638	5.688	0.078
80.0009	−0.108	4.654	1.246
83.3159	−1.519	0.335	0.333
85.6917	−0.546	2.454	−1.212
85.7999	−8.261	2.645	0.726
87.9034	−1.404	2.032	−0.136
89.9920	0.569	1.051	−1.485
92.5032	1.327	4.128	0.684
96.0667	−5.781	1.824	0.909
99.9780	−0.585	1.363	1.151
100.0040	−0.765	1.179	1.535
107.1223	−1.592	5.847	1.040
368.5864	−2.796	0.133	−1.017
637.1940	−2.373	0.996	−0.950
665.9119	−9.823	2.143	0.814
1161.6317	−6.306	4.655	1.130
1513.4660	−8.933	1.988	−0.926
1575.8932	−6.100	5.470	0.826
1673.5069	−10.133	5.812	0.210
1740.4815	−0.283	3.652	0.882
1838.6522	−7.700	1.039	−0.808

B. Outliers

Outliers seen in the stage-0 search are followed up with loose-coherence stages of increasing effective coherence time, as described in section III D, with the SNR expected to increase for true signals. Table V shows the counts of outliers seen at each stage for major sub-bands. In the presence of Gaussian noise and no signal, one expects the outlier counts to decrease monotonically with increasing stage as SNR increases are required for each advancement. For particular sub-bands, however, one can see count increases from at least two contributions, both associated with the finer sampling of parameter space in successive stages. 1) Hardware injections (section III E) from a simulated signal naturally satisfy the SNR increase requirements demanded of a signal; and 2) stationary line artifacts of finite bandwidth can be compatible with signal templates having limited Doppler modulation or having partial cancellation between seasonal modulation and assumed frequency derivative for a certain region of the sky [3].

In the extreme, the number of outliers produced by a particular instrumental artifact can be so large as to make systematic follow-up impracticable and pointless. Table VI shows particular frequency bands (about 13% of the original search band) for which no outlier follow-up is attempted for the initial or later stages because of instrumental artifacts that lead to such an unmanageable flood of initial or later-stage outliers. The table includes the stage for which the vetos are applied in order to reduce artifact-induced outlier counts. Artifacts include loud mechanical resonances, such as higher harmonics of violin modes, and especially loud hardware injections. The widest bands excluded lie in the regions of test-mass violin modes and their higher harmonics. Figure 6 shows these vetoed regions over the full search band, with a magnification of an example 100-Hz band (1900–2000 Hz) that includes a "forest" of 4th harmonics of violin modes from both interferometers. For the narrow search bands affected by loud hardware injections, only outliers within 1.0 radian of the injection's sky location are excluded, except for the top 20 (highest SNR), which are followed up to verify successful injection recovery.

Nearly all outliers that survived all stages of the loose-coherence follow-up correspond to hardware injections (see Table IV) or lie in highly disturbed bands, for which contamination of the putative signal by an instrumental spectral line is apparent. To identify these contaminations, we construct "strain histograms" in which the summed power over the observation period from a simulation of the nominal signal candidate is superposed on a background estimate of the noise estimated via interpolation between neighboring frequency bands. Except for signal templates with high-magnitude spin-downs, the histograms typically display at least one "horn" (narrow peak) from an epoch

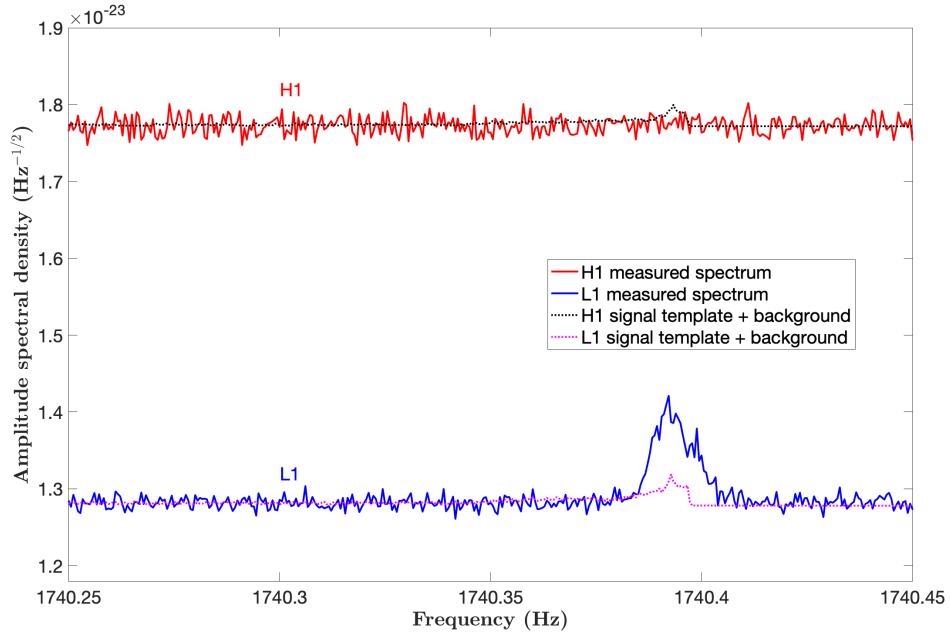

FIG. 7. Example of a "strain histogram" graph used in vetoing outliers surviving stage-2 follow-up for which instrumental contamination is apparent. The solid curves show the O3a-run-averaged H1 (red) and L1 (blue) amplitude spectral densities in a narrow band containing an artifact at 1740.39 Hz. The dotted curves show histograms of expected strain excess from H1 (black) and L1 (magenta) signal templates added to smooth backgrounds interpolated from neighboring frequency bands. In this depiction, the strain amplitude of the signal template has been magnified to make its structure clear. The large excess power in the L1 data, not seen in the H1 data, despite comparable strain sensitivities and comparable sidereal-averaged antenna pattern sensitivities to any point in the sky, excludes an astrophysical source for the L1 artifact. The fact that the artifact aligns in frequency with the putative signal's template peak in power confirms contamination of the outlier from an instrumental source. (color online).

TABLE VIII. Parameters of the outliers surviving stage-2 follow-up and followed up in the full-O3 dataset. Each outlier listed is the loudest after clustering in frequency, spin-down and sky location.

f (Hz)	df/dt (nHz/s)	R.A. (radians)	Dec. (radians)
329.3400	−6.669	5.231	0.531
423.6453	−8.569	5.090	1.067
437.0615	−6.231	0.480	0.613
444.5386	−6.131	6.136	1.160
635.5100	−7.973	3.256	0.116
805.0782	−1.187	0.329	0.912
1150.9380	−8.704	3.895	0.806
1231.9815	−6.154	5.439	1.158
1663.6067	−1.500	6.108	0.331

during the 6-month O3a period when the orbitally modulated frequency is relatively stationary. We discard outliers for which the signal template's shape aligns with a spectral artifact known to be instrumental or appearing loudly in one detector but not the other. Before visual inspection, outliers are clustered in frequency, spin-down and sky location, with the 10 highest-SNR members receiving scrutiny. For reference, Table VII lists the parameters of the single loudest outlier in each cluster discarded after inspecting strain histograms. Figure 7 shows an example of a histogram for an outlier contaminated by an L1 spectral line at 1740.39 Hz.

Any remaining survivors (see Table VIII) are followed up in the full O3 dataset, as described in section III D, and required to yield an SNR increase of at least 20% relative to the original stage-0 values. All but one cluster of outliers fail to satisfy this (conservative) requirement from the fine-grained full-O3 stage-1 follow-up.

The one cluster with (21) full-O3 outliers passing the requirement occurs near 1663.6 Hz (see Table VIII) for which the maximum SNR increase observed is 29%. Examination of the corresponding strain histogram shows evidence of a mild non-Gaussian artifact in L1 data not visible in H1 data, consistent with an instrumental source, but not at a strong enough level to justify visual discarding.

Hence this outlier is subjected to the MCMC PyFstat follow-up procedure described in section III D. The resulting (log) Bayes factor comparing signal to empirical noise expectation for the maximum $\mathcal{F}$-statistic in the last stage is found to be $\log_{10}(B_{\mathrm{SN}}) = 1.1$. Based on the analysis in [41], this value is lower by about 50 than that expected for a standard CW signal of the outlier's putative strain amplitude in the O3a dataset.

We conclude that there is no significant evidence for a continuous wave signal from this search.

V. CONCLUSIONS

We have performed the most sensitive all-sky search to date for continuous gravitational waves in the range 20–2000 Hz while probing spin-down magnitudes as high as 10^{-8} Hz/s, using the PowerFlux search program with loose coherence. The overall improvements in strain sensitivity come primarily from the improved noise floors of the Advanced LIGO interferometers over previous LIGO datasets. Improvements in strain sensitivity over our previous O2 results range from a factor of 1.2 at ∼100 Hz to ∼2 at ∼2000 Hz, with still larger improvements at the lowest frequencies for which spectral line artifacts degraded O2 results.

No credible gravitational wave signals are observed, allowing upper limits to be placed on possible source signal amplitudes. Fig. 4 shows the strain amplitude upper limits obtained. The lowest upper limits on worst-case (linearly polarized) strain amplitude h_0 are $\sim 1.7 \times 10^{-25}$ near 200 Hz. For a circularly polarized source (most favorable orientation), the smallest upper limits are $\sim 6.3 \times 10^{-26}$. These upper limits refer to all sky locations and the entire range of frequency derivative values. For a population-averaged ensemble of sky locations and stellar orientations, the lowest 95% CL upper limits on the strain amplitude are $\sim 1.4 \times 10^{-25}$.

At the highest frequencies (∼2000 Hz) we are sensitive to neutron stars with an equatorial ellipticity ϵ as small as 4×10^{-7} and as far away as 6 kpc for favorable spin orientations (see Fig. 5). For a higher ellipticity $\epsilon = 10^{-6}$ and favorable spin orientations, we are sensitive to neutron stars beyond the galactic center. The maximum ellipticity that a conventional neutron star can theoretically support is at least 1×10^{-5} according to [44,45]. Our results are sensitive to such maximally deformed pulsars above 100 Hz pulsar rotation frequency (200 Hz gravitational-wave frequency) within 3 kpc. Outliers from initial stages of each search method are followed up systematically, but no candidates from any search survived scrutiny.

A recent, similar all-sky search of the LIGO O2 data [15–17], over the same frequency range (20–2000 Hz), but severely restricted in spin-down range ($|\dot{f}| < 3 \times 10^{-12}$ Hz/s), achieved better strain sensitivity (improvements ranging from ∼30% lower at 500 Hz to ∼15% lower at 1500 Hz) by using loose coherence with an effective coherence time of 12 hours in its initial search stage, at a substantially higher computational cost than that of this analysis. A similar approach [18], but further restricting the search frequency range to 171–172 Hz, also achieved a higher sensitivity $h_0 \sim 1.07 \times 10^{-25}$ at 95% confidence. Figure 5 illustrates the potential gain in ellipticity and range sensitivity from searching for high-spin-down magnitudes. A recent deep search of the O2 data using the distributed-computing project Einstein@Home [14] over the frequency band 20–585.15 Hz and spindown magnitude up to 2.6×10^{-9} Hz/s achieved similar sensitivity to this search over the common search parameter space, quoting 90% CL upper limits slightly lower than the 95% CL values presented here. Figure 4 shows the strain upper limits achieved in this O3a

search and in the previous O2 searches, and Fig. 1 shows a comparison of their parameter space coverages.

As the LIGO, Virgo and KAGRA gravitational wave detectors improve their strain sensitivities in the coming decade [46], searches will probe still smaller neutron star deformations and explore further out into the galaxy.

ACKNOWLEDGMENTS

This material is based upon work supported by NSFs LIGO Laboratory which is a major facility fully funded by the National Science Foundation. The authors also gratefully acknowledge the support of the Science and Technology Facilities Council (STFC) of the United Kingdom, the Max-Planck-Society (MPS), and the State of Niedersachsen/Germany for support of the construction of Advanced LIGO and construction and operation of the GEO600 detector. Additional support for Advanced LIGO was provided by the Australian Research Council. The authors gratefully acknowledge the Italian Istituto Nazionale di Fisica Nucleare (INFN), the French Centre National de la Recherche Scientifique (CNRS) and the Netherlands Organization for Scientific Research, for the construction and operation of the Virgo detector and the creation and support of the EGO consortium. The authors also gratefully acknowledge research support from these agencies as well as by the Council of Scientific and Industrial Research of India, the Department of Science and Technology, India, the Science & Engineering Research Board (SERB), India, the Ministry of Human Resource Development, India, the Spanish Agencia Estatal de Investigación, the Vicepresidència i Conselleria d'Innovació, Recerca i Turisme and the Conselleria d'Educació i Universitat del Govern de les Illes Balears, the Conselleria d'Innovació, Universitats, Ciència i Societat Digital de la Generalitat Valenciana and the CERCA Programme Generalitat de Catalunya, Spain, the National Science Centre of Poland and the Foundation for Polish Science (FNP), the Swiss National Science Foundation (SNSF), the Russian Foundation for Basic Research, the Russian Science Foundation, the European Commission, the European Regional Development Funds (ERDF), the Royal Society, the Scottish Funding Council, the Scottish Universities Physics Alliance, the Hungarian Scientific Research Fund (OTKA), the French Lyon Institute of Origins (LIO), the Belgian Fonds de la Recherche Scientifique (FRS-FNRS), Actions de Recherche Concertes (ARC) and Fonds Wetenschappelijk Onderzoek Vlaanderen (FWO), Belgium, the Paris Île-de-France Region, the National Research, Development and Innovation Office Hungary (NKFIH), the National Research Foundation of Korea, the Natural Science and Engineering Research Council Canada, Canadian Foundation for Innovation (CFI), the Brazilian Ministry of Science, Technology, and Innovations, the International Center for Theoretical Physics South American Institute for Fundamental Research (ICTP-SAIFR), the Research Grants Council of Hong Kong, the National Natural Science Foundation of China (NSFC), the Leverhulme Trust, the Research Corporation, the Ministry of Science and Technology (MOST), Taiwan, the United States Department of Energy, and the Kavli Foundation. The authors gratefully acknowledge the support of the NSF, STFC, INFN and CNRS for provision of computational resources. This work was supported by MEXT, JSPS Leading-edge Research Infrastructure Program, JSPS Grant-in-Aid for Specially Promoted Research 26000005, JSPS Grant-in-Aid for Scientific Research on Innovative Areas 2905: JP17H06358, JP17H06361 and JP17H06364, JSPS Core-to-Core Program A. Advanced Research Networks, JSPS Grant-in-Aid for Scientific Research (S) 17H06133, the joint research program of the Institute for Cosmic Ray Research, University of Tokyo, National Research Foundation (NRF) and Computing Infrastructure Project of KISTI-GSDC in Korea, Academia Sinica (AS), AS Grid Center (ASGC) and the Ministry of Science and Technology (MoST) in Taiwan under grants including AS-CDA-105-M06, Advanced Technology Center (ATC) of NAOJ, and Mechanical Engineering Center of KEK. This document has been assigned LIGO Laboratory document number `LIGO-P2000334-v7`.

[1] J. Aasi *et al.* (LIGO Scientific Collaboration), Advanced LIGO, Classical Quantum Gravity **32**, 074001 (2015).

[2] B. P. Abbott *et al.* (LIGO Scientific Collaboration and Virgo Collaboration), GW150914: The Advanced LIGO Detectors in the Era of First Discoveries, Phys. Rev. Lett. **116**, 131103 (2016).

[3] B. P. Abbott *et al.* (LIGO Scientific Collaboration), All-sky search for periodic gravitational waves in LIGO S4 data, Phys. Rev. D **77**, 022001 (2008).

[4] B. P. Abbott *et al.* (LIGO Scientific Collaboration and Virgo Collaboration), All-sky LIGO Search for Periodic Gravitational Waves in the Early S5 Data, Phys. Rev. Lett. **102**, 111102 (2009).

[5] J. Abadie *et al.* (The LIGO and Virgo Scientific Collaboration), All-sky Search for Periodic Gravitational Waves in the Full S5 Data, Phys. Rev. D **85**, 022001 (2012).

[6] B. P. Abbott *et al.* (LIGO Scientific Collaboration and Virgo Collaboration), Comprehensive All-sky search for periodic

gravitational waves in the sixth science run LIGO data, Phys. Rev. D **94**, 042002 (2016).
[7] B. P. Abbott *et al.* (LIGO Scientific Collaboration and Virgo Collaboration), All-sky search for periodic gravitational waves in the O1 LIGO Data, Phys. Rev. D **96**, 062002 (2017).
[8] B. P. Abbott *et al.* (LIGO Scientific Collaboration and Virgo Collaboration), Full band all-sky search for periodic gravitational waves in the O1 LIGO data, Phys. Rev. D **97**, 102003 (2018).
[9] V. Dergachev, On blind searches for noise dominated signals: A loosely coherent approach, Classical Quantum Gravity **27**, 205017 (2010).
[10] V. Dergachev, Loosely coherent searches for sets of well-modeled signals, Phys. Rev. D **85**, 062003 (2012).
[11] B. P. Abbott *et al.* (LIGO Scientific Collaboration and Virgo Collaboration), First low-frequency Einstein@Home all-sky search for continuous gravitational waves in Advanced LIGO data, Phys. Rev. D **96**, 122004 (2017).
[12] B. P. Abbott *et al.* (LIGO Scientific Collaboration and Virgo Collaboration), All-sky search for continuous gravitational waves from isolated neutron stars using Advanced LIGO O2 data Phys. Rev. D **100**, 024004 (2019).
[13] C. Palomba *et al.*, Direct Constraints on Ultra-Light Boson Mass from Searches for Continuous Gravitational Waves, Phys. Rev. Lett. **123**, 171101 (2019).
[14] B. Steltner *et al.*, Einstein@Home all-sky search for continuous gravitational waves in LIGO O2 public data, Astrophys. J. **909**, 79 (2021).
[15] V. Dergachev and M. A. Papa, Results from the First All-Sky Search for Continuous Gravitational Waves from Small-Ellipticity Sources, Phys. Rev. Lett. **125**, 171101 (2020).
[16] V. Dergachev and M. A. Papa, Results from high-frequency all-sky search for continuous gravitational waves from small-ellipticity sources, Phys. Rev. D **103**, 063019 (2021).
[17] V. Dergachev and M. A. Papa, The search for continuous gravitational waves from small-ellipticity sources at low frequencies, arXiv:2104.09007.
[18] K. Wette *et al.*, Deep exploration for continuous gravitational waves at 171–172 Hz in LIGO second observing run data, Phys. Rev. D **103**, 083020 (2021).
[19] M. Tse *et al.*, Quantum-Enhanced Advanced LIGO Detectors in the Era of Gravitational-Wave Astronomy, Phys. Rev. Lett. **123**, 231107 (2019).
[20] P. Lasky, Gravitational waves from neutron stars: A review, Pub. Astron. Soc. Aust. **32**, e034 (2015).
[21] K. Glampedakis and L. Gualtieri, Gravitational waves from single neutron stars: an advanced detector era survey, Astrophysics and Space Science Library **457**, 673 (2018).
[22] B. P. Abbott *et al.* (LIGO Scientific Collaboration and Virgo Collaboration), Observation of Gravitational Waves from a Binary Black Hole Merger, Phys. Rev. Lett. **116**, 061102 (2016).
[23] B. P. Abbott *et al.* (LIGO Scientific Collaboration and Virgo Collaboration), GW170817: Observation of Gravitational Waves from a Binary Neutron Star Inspiral, Phys. Rev. Lett. **119**, 161101 (2017).
[24] B. P. Abbott *et al.* (LIGO Scientific Collaboration and Virgo Collaboration), Binary Black Hole Mergers in the First Advanced LIGO Observing Run, Phys. Rev. X **6**, 041015 (2016).
[25] B. P. Abbott *et al.* (LIGO Scientific Collaboration and Virgo Collaboration), GWTC-1: A Gravitational-Wave Transient Catalog of Compact Binary Mergers Observed by LIGO and Virgo during the First and Second Observing Runs, Phys. Rev. X **9**, 031040 (2019).
[26] B. P. Abbott *et al.* (LIGO Scientific Collaboration and Virgo Collaboration), GWTC-2: Compact Binary Coalescences Observed by LIGO and Virgo During the First Half of the Third Observing Run, Phys. Rev. X **11**, 021053 (2021).
[27] B. P. Abbott *et al.* (LIGO Scientific Collaboration and Virgo Collaboration), GW190425: Observation of a compact binary coalescence with total mass ∼3.4 Msun, Astrophys. J. Lett. **892**, L3 (2020).
[28] B. P. Abbott *et al.* (LIGO Scientific Collaboration and Virgo Collaboration), GW190814: Gravitational waves from the coalescence of a 23 solar mass black hole with a 2.6 solar mass compact object, Astrophys. J. Lett. **896**, L44 (2020).
[29] F. Acernese *et al.*, Advanced Virgo: A 2nd generation interferometric gravitational wave detector, Classical Quantum Gravity **32**, 024001 (2015).
[30] P. Covas *et al.*, Identification and mitigation of narrow spectral artifacts that degrade searches for persistent gravitational waves in the first two observing runs of Advanced LIGO, Phys. Rev. D **97**, 082002 (2018).
[31] E. Goetz *et al.*, O3a lines and combs in C00 data, https://dcc.ligo.org/LIGO-T2000719-v1.
[32] J. Zweizig and K. Riles, Information on self-gating of $h(t)$ used in O3a continuous-wave searches,. LIGO Technical Report No. T2000384, 2020, https://dcc.ligo.org/LIGO-T2000384.
[33] D. Davis *et al.*, LIGO detector characterization in the second and third observing runs, Classical Quantum Gravity **38**, 135014 (2021).
[34] L. Sun *et al.*, Characterization of systematic error in Advanced LIGO calibration, Classical Quantum Gravity **37**, 225008 (2020).
[35] A. Arvanitaki and S. Dubovsky, Exploring the string axiverse with precision black holephysics, Phys. Rev. D **83**, 044026 (2011).
[36] B. P. Abbott *et al.* (LIGO Scientific Collaboration and Virgo Collaboration), Searches for gravitational waves from known pulsars at two harmonics in 2015-2017 LIGO data, Astrophys. J. **879**, 10 (2019).
[37] V. Dergachev, A novel universal statistic for computing upper limits in Ill-behaved Background, Phys. Rev. D **87**, 062001 (2013).
[38] D. Keitel, R. Tenorio, G. Ashton, and R. Prix, PyFstat: a Python package for continuous gravitational-wave data analysis, J. Open Source Software **6**, 3000 (2021).
[39] G. Ashton, D. Keitel, R. Prix, and R. Tenorio, PyFstat v.1.11.3, Zenodo, https://doi.org/10.5281/zenodo.4542822.
[40] G. Ashton and R. Prix, Hierarchical multistage MCMC follow-up of continuous gravitational wave candidates, Phys. Rev. D **97**, 103020 (2018).
[41] R. Tenorio, D. Keitel, and A. M. Sintes, Application of a hierarchical MCMC follow-up to Advanced LIGO continuous gravitational-wave candidates, Phys. Rev. D **104**, 084012 (2021).

[42] P. Jaranowski, A. Krolak, and B. F. Schutz, Data analysis of gravitational-wave signals from spinning neutron stars. 1. The Signal and its detection, Phys. Rev. D **58**, 063001 (1998).
[43] C. Biwer *et al.*, Validating gravitational-wave detections: The Advanced LIGO hardware injection system, Phys. Rev. D **95**, 062002 (2017).
[44] C. J. Horowitz and K. Kadau, Breaking Strain of Neutron Star Crust and Gravitational Waves, Phys. Rev. Lett. **102**, 191102 (2009).
[45] N. K. Johnson-McDaniel and B. J. Owen, Maximum elastic deformations of relativistic stars, Phys. Rev. D **88**, 044004 (2013).
[46] B. P. Abbott *et al.* (KAGRA Collaboration, LIGO Scientific Collaboration and Virgo Collaboration), Prospects for observing and localizing gravitational-wave transients with Advanced LIGO, Advanced Virgo and KAGRA, Living Rev. Relativity **23**, 3 (2020).

R. Abbott,[1] T. D. Abbott,[2] S. Abraham,[3] F. Acernese,[4,5] K. Ackley,[6] A. Adams,[7] C. Adams,[8] R. X. Adhikari,[1] V. B. Adya,[9] C. Affeldt,[10,11] D. Agarwal,[3] M. Agathos,[12,13] K. Agatsuma,[14] N. Aggarwal,[15] O. D. Aguiar,[16] L. Aiello,[17,18,19] A. Ain,[20,21] P. Ajith,[22] T. Akutsu,[23,24] K. M. Aleman,[25] G. Allen,[26] A. Allocca,[27,5] P. A. Altin,[9] A. Amato,[28] S. Anand,[1] A. Ananyeva,[1] S. B. Anderson,[1] W. G. Anderson,[29] M. Ando,[30,31] S. V. Angelova,[32] S. Ansoldi,[33,34] J. M. Antelis,[35] S. Antier,[36] S. Appert,[1] Koya Arai,[37] Koji Arai,[1] Y. Arai,[37] S. Araki,[38] A. Araya,[39] M. C. Araya,[1] J. S. Areeda,[25] M. Arène,[36] N. Aritomi,[30] N. Arnaud,[40,41] S. M. Aronson,[42] H. Asada,[43] Y. Asali,[44] G. Ashton,[6] Y. Aso,[45,46] S. M. Aston,[8] P. Astone,[47] F. Aubin,[48] P. Aufmuth,[10,11] K. AultONeal,[35] C. Austin,[2] S. Babak,[36] F. Badaracco,[18,19] M. K. M. Bader,[49] S. Bae,[50] Y. Bae,[51] A. M. Baer,[7] S. Bagnasco,[52] Y. Bai,[1] L. Baiotti,[53] J. Baird,[36] R. Bajpai,[54] M. Ball,[55] G. Ballardin,[41] S. W. Ballmer,[56] M. Bals,[35] A. Balsamo,[7] G. Baltus,[57] S. Banagiri,[58] D. Bankar,[3] R. S. Bankar,[3] J. C. Barayoga,[1] C. Barbieri,[59,60,61] B. C. Barish,[1] D. Barker,[62] P. Barneo,[63] F. Barone,[64,5] B. Barr,[65] L. Barsotti,[66] M. Barsuglia,[36] D. Barta,[67] J. Bartlett,[62] M. A. Barton,[65,23] I. Bartos,[42] R. Bassiri,[68] A. Basti,[21,20] M. Bawaj,[69,70] J. C. Bayley,[65] A. C. Baylor,[29] M. Bazzan,[71,72] B. Bécsy,[73] V. M. Bedakihale,[74] M. Bejger,[75] I. Belahcene,[40] V. Benedetto,[76] D. Beniwal,[77] M. G. Benjamin,[35] T. F. Bennett,[78] J. D. Bentley,[14] M. BenYaala,[32] F. Bergamin,[10,11] B. K. Berger,[68] S. Bernuzzi,[13] D. Bersanetti,[79] A. Bertolini,[49] J. Betzwieser,[8] R. Bhandare,[80] A. V. Bhandari,[3] D. Bhattacharjee,[81] S. Bhaumik,[42] J. Bidler,[25] I. A. Bilenko,[82] G. Billingsley,[1] R. Birney,[83] O. Birnholtz,[84] S. Biscans,[1,66] M. Bischi,[85,86] S. Biscoveanu,[66] A. Bisht,[10,11] B. Biswas,[3] M. Bitossi,[41,20] M.-A. Bizouard,[87] J. K. Blackburn,[1] J. Blackman,[88] C. D. Blair,[89,8] D. G. Blair,[89] R. M. Blair,[62] F. Bobba,[90,91] N. Bode,[10,11] M. Boer,[87] G. Bogaert,[87] M. Boldrini,[92,47] F. Bondu,[93] E. Bonilla,[68] R. Bonnand,[48] P. Booker,[10,11] B. A. Boom,[49] R. Bork,[1] V. Boschi,[20] N. Bose,[94] S. Bose,[3] V. Bossilkov,[89] V. Boudart,[57] Y. Bouffanais,[71,72] A. Bozzi,[41] C. Bradaschia,[20] P. R. Brady,[29] A. Bramley,[8] A. Branch,[8] M. Branchesi,[18,19] J. E. Brau,[55] M. Breschi,[13] T. Briant,[95] J. H. Briggs,[65] A. Brillet,[87] M. Brinkmann,[10,11] P. Brockill,[29] A. F. Brooks,[1] J. Brooks,[41] D. D. Brown,[77] S. Brunett,[1] G. Bruno,[96] R. Bruntz,[7] J. Bryant,[14] A. Buikema,[66] T. Bulik,[97] H. J. Bulten,[49,98] A. Buonanno,[99,100] R. Buscicchio,[14] D. Buskulic,[48] R. L. Byer,[68] L. Cadonati,[101] M. Caesar,[102] G. Cagnoli,[28] C. Cahillane,[1] H. W. Cain III,[2] J. Calderón Bustillo,[103] J. D. Callaghan,[65] T. A. Callister,[104,105] E. Calloni,[27,5] J. B. Camp,[106] M. Canepa,[107,79] M. Cannavacciuolo,[90] K. C. Cannon,[31] H. Cao,[77] J. Cao,[108] Z. Cao,[109] E. Capocasa,[23] E. Capote,[25] G. Carapella,[90,91] F. Carbognani,[41] J. B. Carlin,[110] M. F. Carney,[15] M. Carpinelli,[111,112] G. Carullo,[21,20] T. L. Carver,[17] J. Casanueva Diaz,[41] C. Casentini,[113,114] G. Castaldi,[115] S. Caudill,[49,116] M. Cavaglià,[81] F. Cavalier,[40] R. Cavalieri,[41] G. Cella,[20] P. Cerdá-Durán,[117] E. Cesarini,[114] W. Chaibi,[87] K. Chakravarti,[3] B. Champion,[118] C.-H. Chan,[119] C. Chan,[31] C. L. Chan,[103] M. Chan,[120] K. Chandra,[94] P. Chanial,[41] S. Chao,[119] P. Charlton,[121] E. A. Chase,[15] E. Chassande-Mottin,[36] D. Chatterjee,[29] M. Chaturvedi,[80] A. Chen,[103] C. Chen,[122,123] H. Y. Chen,[124] J. Chen,[119] K. Chen,[125] X. Chen,[89] Y.-B. Chen,[88] Y.-R. Chen,[123] Z. Chen,[17] H. Cheng,[42] C. K. Cheong,[103] H. Y. Cheung,[103] H. Y. Chia,[42] F. Chiadini,[126,91] C-Y. Chiang,[127] R. Chierici,[128] A. Chincarini,[79] M. L. Chiofalo,[21,20] A. Chiummo,[41] G. Cho,[129] H. S. Cho,[130] S. Choate,[102] R. K. Choudhary,[89] S. Choudhary,[3] N. Christensen,[87] H. Chu,[125] Q. Chu,[89] Y-K. Chu,[127] S. Chua,[95] K. W. Chung,[131] G. Ciani,[71,72] P. Ciecielag,[75] M. Cieślar,[75] M. Cifaldi,[113,114] A. A. Ciobanu,[77] R. Ciolfi,[132,72] F. Cipriano,[87] A. Cirone,[107,79] F. Clara,[62] E. N. Clark,[133] J. A. Clark,[101] L. Clarke,[134] P. Clearwater,[110] S. Clesse,[135] F. Cleva,[87] E. Coccia,[18,19] P.-F. Cohadon,[95] D. E. Cohen,[40] L. Cohen,[2] M. Colleoni,[136] C. G. Collette,[137] M. Colpi,[59,60] C. M. Compton,[62] M. Constancio Jr.,[16] L. Conti,[72] S. J. Cooper,[14] P. Corban,[8] T. R. Corbitt,[2] I. Cordero-Carrión,[138] S. Corezzi,[70,69] K. R. Corley,[44] N. Cornish,[73] D. Corre,[40] A. Corsi,[139] S. Cortese,[41] C. A. Costa,[16] R. Cotesta,[100] M. W. Coughlin,[58] S. B. Coughlin,[15,17] J.-P. Coulon,[87] S. T. Countryman,[44] B. Cousins,[140] P. Couvares,[1] P. B. Covas,[136] D. M. Coward,[89] M. J. Cowart,[8] D. C. Coyne,[1] R. Coyne,[141]

J. D. E. Creighton,[29] T. D. Creighton,[142] A. W. Criswell,[58] M. Croquette,[95] S. G. Crowder,[143] J. R. Cudell,[57] T. J. Cullen,[2] A. Cumming,[65] R. Cummings,[65] E. Cuoco,[41,144,20] M. Curyło,[97] T. Dal Canton,[100,40] G. Dálya,[145] A. Dana,[68] L. M. DaneshgaranBajastani,[78] B. D'Angelo,[107,79] S. L. Danilishin,[146] S. D'Antonio,[114] K. Danzmann,[10,11] C. Darsow-Fromm,[147] A. Dasgupta,[74] L. E. H. Datrier,[65] V. Dattilo,[41] I. Dave,[80] M. Davier,[40] G. S. Davies,[148,149] D. Davis,[1] E. J. Daw,[150] R. Dean,[102] D. DeBra,[68] M. Deenadayalan,[3] J. Degallaix,[151] M. De Laurentis,[27,5] S. Deléglise,[95] V. Del Favero,[118] F. De Lillo,[96] N. De Lillo,[65] W. Del Pozzo,[21,20] L. M. DeMarchi,[15] F. De Matteis,[113,114] V. D'Emilio,[17] N. Demos,[66] T. Dent,[148] A. Depasse,[96] R. De Pietri,[152,153] R. De Rosa,[27,5] C. De Rossi,[41] R. DeSalvo,[115] R. De Simone,[126] S. Dhurandhar,[3] M. C. Díaz,[142] M. Diaz-Ortiz Jr.,[42] N. A. Didio,[56] T. Dietrich,[100] L. Di Fiore,[5] C. Di Fronzo,[14] C. Di Giorgio,[90,91] F. Di Giovanni,[117] T. Di Girolamo,[27,5] A. Di Lieto,[21,20] B. Ding,[137] S. Di Pace,[92,47] I. Di Palma,[92,47] F. Di Renzo,[21,20] A. K. Divakarla,[42] A. Dmitriev,[14] Z. Doctor,[55] L. D'Onofrio,[27,5] F. Donovan,[66] K. L. Dooley,[17] S. Doravari,[3] I. Dorrington,[17] M. Drago,[18,19] J. C. Driggers,[62] Y. Drori,[1] Z. Du,[108] J.-G. Ducoin,[40] P. Dupej,[65] O. Durante,[90,91] D. D'Urso,[111,112] P.-A. Duverne,[40] S. E. Dwyer,[62] P. J. Easter,[6] M. Ebersold,[154] G. Eddolls,[65] B. Edelman,[55] T. B. Edo,[1,150] O. Edy,[149] A. Effler,[8] S. Eguchi,[120] J. Eichholz,[9] S. S. Eikenberry,[42] M. Eisenmann,[48] R. A. Eisenstein,[66] A. Ejlli,[17] Y. Enomoto,[30] L. Errico,[27,5] R. C. Essick,[124] H. Estellés,[136] D. Estevez,[155] Z. Etienne,[156] T. Etzel,[1] M. Evans,[66] T. M. Evans,[8] B. E. Ewing,[140] V. Fafone,[113,114,18] H. Fair,[56] S. Fairhurst,[17] X. Fan,[108] A. M. Farah,[124] S. Farinon,[79] B. Farr,[55] W. M. Farr,[104,105] N. W. Farrow,[6] E. J. Fauchon-Jones,[17] M. Favata,[157] M. Fays,[57,150] M. Fazio,[158] J. Feicht,[1] M. M. Fejer,[68] F. Feng,[36] E. Fenyvesi,[67,159] D. L. Ferguson,[101] A. Fernandez-Galiana,[66] I. Ferrante,[21,20] T. A. Ferreira,[16] F. Fidecaro,[21,20] P. Figura,[97] I. Fiori,[41] M. Fishbach,[15,124] R. P. Fisher,[7] R. Fittipaldi,[160,91] V. Fiumara,[161,91] R. Flaminio,[48,23] E. Floden,[58] E. Flynn,[25] H. Fong,[31] J. A. Font,[117,162] B. Fornal,[163] P. W. F. Forsyth,[9] A. Franke,[147] S. Frasca,[92,47] F. Frasconi,[20] C. Frederick,[164] Z. Frei,[145] A. Freise,[165] R. Frey,[55] P. Fritschel,[66] V. V. Frolov,[8] G. G. Fronzé,[52] Y. Fujii,[166] Y. Fujikawa,[167] M. Fukunaga,[37] M. Fukushima,[24] P. Fulda,[42] M. Fyffe,[8] H. A. Gabbard,[65] B. U. Gadre,[100] S. M. Gaebel,[14] J. R. Gair,[100] J. Gais,[103] S. Galaudage,[6] R. Gamba,[13] D. Ganapathy,[66] A. Ganguly,[22] D. Gao,[168] S. G. Gaonkar,[3] B. Garaventa,[79,107] C. García-Núñez,[83] C. García-Quirós,[136] F. Garufi,[27,5] B. Gateley,[62] S. Gaudio,[35] V. Gayathri,[42] G. Ge,[168] G. Gemme,[79] A. Gennai,[20] J. George,[80] L. Gergely,[169] P. Gewecke,[147] S. Ghonge,[101] Abhirup. Ghosh,[100] Archisman Ghosh,[170] Shaon Ghosh,[29,157] Shrobana Ghosh,[17] Sourath Ghosh,[42] B. Giacomazzo,[59,60,61] L. Giacoppo,[92,47] J. A. Giaime,[2,8] K. D. Giardina,[8] D. R. Gibson,[83] C. Gier,[32] M. Giesler,[88] P. Giri,[20,21] F. Gissi,[76] J. Glanzer,[2] A. E. Gleckl,[25] P. Godwin,[140] E. Goetz,[171] R. Goetz,[42] N. Gohlke,[10,11] B. Goncharov,[6] G. González,[2] A. Gopakumar,[172] M. Gosselin,[41] R. Gouaty,[48] B. Grace,[9] A. Grado,[173,5] M. Granata,[151] V. Granata,[90] A. Grant,[65] S. Gras,[66] P. Grassia,[1] C. Gray,[62] R. Gray,[65] G. Greco,[69] A. C. Green,[42] R. Green,[17] A. M. Gretarsson,[35] E. M. Gretarsson,[35] D. Griffith,[1] W. Griffiths,[17] H. L. Griggs,[101] G. Grignani,[70,69] A. Grimaldi,[174,175] E. Grimes,[35] S. J. Grimm,[18,19] H. Grote,[17] S. Grunewald,[100] P. Gruning,[40] J. G. Guerrero,[25] G. M. Guidi,[85,86] A. R. Guimaraes,[2] G. Guixé,[63] H. K. Gulati,[74] H.-K. Guo,[163] Y. Guo,[49] Anchal Gupta,[1] Anuradha Gupta,[176] P. Gupta,[49,116] E. K. Gustafson,[1] R. Gustafson,[177] F. Guzman,[133] S. Ha,[178] L. Haegel,[36] A. Hagiwara,[37,179] S. Haino,[127] O. Halim,[180,34] E. D. Hall,[66] E. Z. Hamilton,[17] G. Hammond,[65] W.-B. Han,[181] M. Haney,[154] J. Hanks,[62] C. Hanna,[140] M. D. Hannam,[17] O. A. Hannuksela,[116,49,103] H. Hansen,[62] T. J. Hansen,[35] J. Hanson,[8] T. Harder,[87] T. Hardwick,[2] K. Haris,[49,116,22] J. Harms,[18,19] G. M. Harry,[182] I. W. Harry,[149] D. Hartwig,[147] K. Hasegawa,[37] B. Haskell,[75] R. K. Hasskew,[8] C.-J. Haster,[66] K. Hattori,[183] K. Haughian,[65] H. Hayakawa,[184] K. Hayama,[120] F. J. Hayes,[65] J. Healy,[118] A. Heidmann,[95] M. C. Heintze,[8] J. Heinze,[10,11] J. Heinzel,[185] H. Heitmann,[87] F. Hellman,[186] P. Hello,[40] A. F. Helmling-Cornell,[55] G. Hemming,[41] M. Hendry,[65] I. S. Heng,[65] E. Hennes,[49] J. Hennig,[10,11] M. H. Hennig,[10,11] F. Hernandez Vivanco,[6] M. Heurs,[10,11] S. Hild,[146,49] P. Hill,[32] Y. Himemoto,[187] A. S. Hines,[133] Y. Hiranuma,[188] N. Hirata,[23] E. Hirose,[37] S. Hochheim,[10,11] D. Hofman,[151] J. N. Hohmann,[147] A. M. Holgado,[26] N. A. Holland,[9] I. J. Hollows,[150] Z. J. Holmes,[77] K. Holt,[8] D. E. Holz,[124] Z. Hong,[189] P. Hopkins,[17] J. Hough,[65] E. J. Howell,[89] C. G. Hoy,[17] D. Hoyland,[14] A. Hreibi,[10,11] B-H. Hsieh,[37] Y. Hsu,[119] G-Z. Huang,[189] H-Y. Huang,[127] P. Huang,[168] Y-C. Huang,[123] Y.-J. Huang,[127] Y.-W. Huang,[66] M. T. Hübner,[6] A. D. Huddart,[134] E. A. Huerta,[26] B. Hughey,[35] D. C. Y. Hui,[190] V. Hui,[48] S. Husa,[136] S. H. Huttner,[65] R. Huxford,[140] T. Huynh-Dinh,[8] S. Ide,[191] B. Idzkowski,[97] A. Iess,[113,114] B. Ikenoue,[24] S. Imam,[189] K. Inayoshi,[192] H. Inchauspe,[42] C. Ingram,[77] Y. Inoue,[125] G. Intini,[92,47] K. Ioka,[193] M. Isi,[66] K. Isleif,[147] K. Ito,[194] Y. Itoh,[195,196] B. R. Iyer,[22] K. Izumi,[197] V. JaberianHamedan,[89] T. Jacqmin,[95] S. J. Jadhav,[198] S. P. Jadhav,[3] A. L. James,[17] A. Z. Jan,[118] K. Jani,[101] K. Janssens,[199] N. N. Janthalur,[198] P. Jaranowski,[200] D. Jariwala,[42] R. Jaume,[136] A. C. Jenkins,[131] C. Jeon,[201] M. Jeunon,[58] W. Jia,[66] J. Jiang,[42] H.-B. Jin,[202,203] G. R. Johns,[7] A. W. Jones,[89] D. I. Jones,[204] J. D. Jones,[62] P. Jones,[14] R. Jones,[65] R. J. G. Jonker,[49] L. Ju,[89] K. Jung,[178] P. Jung,[184] J. Junker,[10,11] K. Kaihotsu,[194] T. Kajita,[205]

M. Kakizaki,[183] C. V. Kalaghatgi,[17] V. Kalogera,[15] B. Kamai,[1] M. Kamiizumi,[184] N. Kanda,[195,196] S. Kandhasamy,[3] G. Kang,[50] J. B. Kanner,[1] Y. Kao,[119] S. J. Kapadia,[22] D. P. Kapasi,[9] S. Karat,[1] C. Karathanasis,[206] S. Karki,[81] R. Kashyap,[140] M. Kasprzack,[1] W. Kastaun,[10,11] S. Katsanevas,[41] E. Katsavounidis,[66] W. Katzman,[8] T. Kaur,[89] K. Kawabe,[62] K. Kawaguchi,[37] N. Kawai,[207] T. Kawasaki,[30] F. Kéfélian,[87] D. Keitel,[136] J. S. Key,[208] S. Khadka,[68] F. Y. Khalili,[82] I. Khan,[18,114] S. Khan,[17] E. A. Khazanov,[209] N. Khetan,[18,19] M. Khursheed,[80] N. Kijbunchoo,[9] C. Kim,[210,201] J. C. Kim,[211] J. Kim,[212] K. Kim,[213] W. S. Kim,[51] Y.-M. Kim,[178] C. Kimball,[15] N. Kimura,[179] P. J. King,[62] M. Kinley-Hanlon,[65] R. Kirchhoff,[10,11] J. S. Kissel,[62] N. Kita,[30] H. Kitazawa,[194] L. Kleybolte,[147] S. Klimenko,[42] A. M. Knee,[171] T. D. Knowles,[156] E. Knyazev,[66] P. Koch,[10,11] G. Koekoek,[49,146] Y. Kojima,[214] K. Kokeyama,[184] S. Koley,[49] P. Kolitsidou,[17] M. Kolstein,[206] K. Komori,[66,30] V. Kondrashov,[1] A. K. H. Kong,[123] A. Kontos,[215] N. Koper,[10,11] M. Korobko,[147] K. Kotake,[120] M. Kovalam,[89] D. B. Kozak,[1] C. Kozakai,[45] R. Kozu,[216] V. Kringel,[10,11] N. V. Krishnendu,[10,11] A. Królak,[217,218] G. Kuehn,[10,11] F. Kuei,[119] A. Kumar,[198] P. Kumar,[219] Rahul Kumar,[62] Rakesh Kumar,[74] J. Kume,[31] K. Kuns,[66] C. Kuo,[125] H-S. Kuo,[189] Y. Kuromiya,[194] S. Kuroyanagi,[220] K. Kusayanagi,[207] K. Kwak,[178] S. Kwang,[29] D. Laghi,[21,20] E. Lalande,[221] T. L. Lam,[103] A. Lamberts,[87,222] M. Landry,[62] B. B. Lane,[66] R. N. Lang,[66] J. Lange,[223,118] B. Lantz,[68] I. La Rosa,[48] A. Lartaux-Vollard,[40] P. D. Lasky,[6] M. Laxen,[8] A. Lazzarini,[1] C. Lazzaro,[71,72] P. Leaci,[92,47] S. Leavey,[10,11] Y. K. Lecoeuche,[62] H. K. Lee,[224] H. M. Lee,[213] H. W. Lee,[211] J. Lee,[129] K. Lee,[68] R. Lee,[123] J. Lehmann,[10,11] A. Lemaître,[225] E. Leon,[25] M. Leonardi,[23] N. Leroy,[40] N. Letendre,[48] Y. Levin,[6] J. N. Leviton,[177] A. K. Y. Li,[1] B. Li,[119] J. Li,[15] K. L. Li,[123] T. G. F. Li,[103] X. Li,[88] C-Y. Lin,[226] F-K. Lin,[127] F-L. Lin,[189] H. L. Lin,[125] L. C.-C. Lin,[178] F. Linde,[227,49] S. D. Linker,[78] J. N. Linley,[65] T. B. Littenberg,[228] G. C. Liu,[122] J. Liu,[10,11] K. Liu,[119] X. Liu,[29] M. Llorens-Monteagudo,[117] R. K. L. Lo,[1] A. Lockwood,[229] M. L. Lollie,[2] L. T. London,[66] A. Longo,[230,231] D. Lopez,[154] M. Lorenzini,[113,114] V. Loriette,[232] M. Lormand,[8] G. Losurdo,[20] J. D. Lough,[10,11] C. O. Lousto,[118] G. Lovelace,[25] H. Lück,[10,11] D. Lumaca,[113,114] A. P. Lundgren,[149] L.-W. Luo,[127] R. Macas,[17] M. MacInnis,[66] D. M. Macleod,[17] I. A. O. MacMillan,[1] A. Macquet,[87] I. Magaña Hernandez,[29] F. Magaña-Sandoval,[42] C. Magazzù,[20] R. M. Magee,[140] R. Maggiore,[14] E. Majorana,[92,47] C. Makarem,[1] I. Maksimovic,[232] S. Maliakal,[1] A. Malik,[80] N. Man,[87] V. Mandic,[58] V. Mangano,[92,47] J. L. Mango,[233] G. L. Mansell,[62,66] M. Manske,[29] M. Mantovani,[41] M. Mapelli,[71,72] F. Marchesoni,[234,69] M. Marchio,[23] F. Marion,[48] Z. Mark,[88] S. Márka,[44] Z. Márka,[44] C. Markakis,[12] A. S. Markosyan,[68] A. Markowitz,[1] E. Maros,[1] A. Marquina,[138] S. Marsat,[36] F. Martelli,[85,86] I. W. Martin,[65] R. M. Martin,[157] M. Martinez,[206] V. Martinez,[28] K. Martinovic,[131] D. V. Martynov,[14] E. J. Marx,[66] H. Masalehdan,[147] K. Mason,[66] E. Massera,[150] A. Masserot,[48] T. J. Massinger,[66] M. Masso-Reid,[65] S. Mastrogiovanni,[36] A. Matas,[100] M. Mateu-Lucena,[136] F. Matichard,[1,66] M. Matiushechkina,[10,11] N. Mavalvala,[66] J. J. McCann,[89] R. McCarthy,[62] D. E. McClelland,[9] P. McClincy,[140] S. McCormick,[8] L. McCuller,[66] G. I. McGhee,[65] S. C. McGuire,[235] C. McIsaac,[149] J. McIver,[171] D. J. McManus,[9] T. McRae,[9] S. T. McWilliams,[156] D. Meacher,[29] M. Mehmet,[10,11] A. K. Mehta,[100] A. Melatos,[110] D. A. Melchor,[25] G. Mendell,[62] A. Menendez-Vazquez,[206] C. S. Menoni,[158] R. A. Mercer,[29] L. Mereni,[151] K. Merfeld,[55] E. L. Merilh,[62] J. D. Merritt,[55] M. Merzougui,[87] S. Meshkov,[1,a] C. Messenger,[65] C. Messick,[223] P. M. Meyers,[110] F. Meylahn,[10,11] A. Mhaske,[3] A. Miani,[174,175] H. Miao,[14] I. Michaloliakos,[42] C. Michel,[151] Y. Michimura,[30] H. Middleton,[110] L. Milano,[27] A. L. Miller,[96,42] M. Millhouse,[110] J. C. Mills,[17] E. Milotti,[180,34] M. C. Milovich-Goff,[78] O. Minazzoli,[87,236] Y. Minenkov,[114] N. Mio,[237] Ll. M. Mir,[206] A. Mishkin,[42] C. Mishra,[238] T. Mishra,[42] T. Mistry,[150] S. Mitra,[3] V. P. Mitrofanov,[82] G. Mitselmakher,[42] R. Mittleman,[66] O. Miyakawa,[184] A. Miyamoto,[195] Y. Miyazaki,[30] K. Miyo,[184] S. Miyoki,[184] Geoffrey Mo,[66] K. Mogushi,[81] S. R. P. Mohapatra,[66] S. R. Mohite,[29] I. Molina,[25] M. Molina-Ruiz,[186] M. Mondin,[78] M. Montani,[85,86] C. J. Moore,[14] D. Moraru,[62] F. Morawski,[75] A. More,[3] C. Moreno,[35] G. Moreno,[62] Y. Mori,[194] S. Morisaki,[31,37] Y. Moriwaki,[183] B. Mours,[155] C. M. Mow-Lowry,[14] S. Mozzon,[149] F. Muciaccia,[92,47] Arunava Mukherjee,[239,65] D. Mukherjee,[140] Soma Mukherjee,[142] Subroto Mukherjee,[74] N. Mukund,[10,11] A. Mullavey,[8] J. Munch,[77] E. A. Muñiz,[56] P. G. Murray,[65] R. Musenich,[79,107] S. L. Nadji,[10,11] K. Nagano,[197] S. Nagano,[240] A. Nagar,[52,241] K. Nakamura,[23] H. Nakano,[242] M. Nakano,[37] R. Nakashima,[207] Y. Nakayama,[183] I. Nardecchia,[113,114] T. Narikawa,[37] L. Naticchioni,[47] B. Nayak,[78] R. K. Nayak,[243] R. Negishi,[188] B. F. Neil,[89] J. Neilson,[76,91] G. Nelemans,[244] T. J. N. Nelson,[8] M. Nery,[10,11] A. Neunzert,[208] K. Y. Ng,[66] S. W. S. Ng,[77] C. Nguyen,[36] P. Nguyen,[55] T. Nguyen,[66] L. Nguyen Quynh,[245] W.-T. Ni,[202,168,246] S. A. Nichols,[2] A. Nishizawa,[31] S. Nissanke,[247,49] F. Nocera,[41] M. Noh,[171] M. Norman,[17] C. North,[17] S. Nozaki,[183] L. K. Nuttall,[149] J. Oberling,[62] B. D. O'Brien,[42] Y. Obuchi,[24] J. O'Dell,[134] W. Ogaki,[37] G. Oganesyan,[18,19] J. J. Oh,[51] K. Oh,[190] S. H. Oh,[51] M. Ohashi,[184] N. Ohishi,[45] M. Ohkawa,[167] F. Ohme,[10,11] H. Ohta,[31] M. A. Okada,[16] Y. Okutani,[191] K. Okutomi,[184] C. Olivetto,[41] K. Oohara,[188] C. Ooi,[30] R. Oram,[8] B. O'Reilly,[8] R. G. Ormiston,[58] N. D. Ormsby,[7] L. F. Ortega,[42]

R. O'Shaughnessy,[118] E. O'Shea,[219] S. Oshino,[184] S. Ossokine,[100] C. Osthelder,[1] S. Otabe,[207] D. J. Ottaway,[77] H. Overmier,[8] A. E. Pace,[140] G. Pagano,[21,20] M. A. Page,[89] G. Pagliaroli,[18,19] A. Pai,[94] S. A. Pai,[80] J. R. Palamos,[55] O. Palashov,[209] C. Palomba,[47] K. Pan,[123] P. K. Panda,[198] H. Pang,[125] P. T. H. Pang,[49,116] C. Pankow,[15] F. Pannarale,[92,47] B. C. Pant,[80] F. Paoletti,[20] A. Paoli,[41] A. Paolone,[47,248] A. Parisi,[122] J. Park,[213] W. Parker,[8,235] D. Pascucci,[49] A. Pasqualetti,[41] R. Passaquieti,[21,20] D. Passuello,[20] M. Patel,[7] B. Patricelli,[41,20] E. Payne,[6] T. C. Pechsiri,[42] M. Pedraza,[1] M. Pegoraro,[72] A. Pele,[8] F. E. Peña Arellano,[184] S. Penn,[249] A. Perego,[174,175] A. Pereira,[28] T. Pereira,[250] C. J. Perez,[62] C. Périgois,[48] A. Perreca,[174,175] S. Perriès,[128] J. Petermann,[147] D. Petterson,[1] H. P. Pfeiffer,[100] K. A. Pham,[58] K. S. Phukon,[49,227,3] O. J. Piccinni,[47] M. Pichot,[87] M. Piendibene,[21,20] F. Piergiovanni,[85,86] L. Pierini,[92,47] V. Pierro,[76,91] G. Pillant,[41] F. Pilo,[20] L. Pinard,[151] I. M. Pinto,[76,91,251,252] B. J. Piotrzkowski,[29] K. Piotrzkowski,[96] M. Pirello,[62] M. Pitkin,[253] E. Placidi,[92,47] W. Plastino,[230,231] C. Pluchar,[133] R. Poggiani,[21,20] E. Polini,[48] D. Y. T. Pong,[103] S. Ponrathnam,[3] P. Popolizio,[41] E. K. Porter,[36] J. Powell,[254] M. Pracchia,[48] T. Pradier,[155] A. K. Prajapati,[74] K. Prasai,[68] R. Prasanna,[198] G. Pratten,[14] T. Prestegard,[29] M. Principe,[76,251,91] G. A. Prodi,[255,175] L. Prokhorov,[14] P. Prosposito,[113,114] L. Prudenzi,[100] A. Puecher,[49,116] M. Punturo,[69] F. Puosi,[20,21] P. Puppo,[47] M. Pürrer,[100] H. Qi,[17] V. Quetschke,[142] P. J. Quinonez,[35] R. Quitzow-James,[81] F. J. Raab,[62] G. Raaijmakers,[247,49] H. Radkins,[62] N. Radulesco,[87] P. Raffai,[145] S. X. Rail,[221] S. Raja,[80] C. Rajan,[80] K. E. Ramirez,[142] T. D. Ramirez,[25] A. Ramos-Buades,[100] J. Rana,[140] P. Rapagnani,[92,47] U. D. Rapol,[256] B. Ratto,[35] V. Raymond,[17] N. Raza,[171] M. Razzano,[21,20] J. Read,[25] L. A. Rees,[182] T. Regimbau,[48] L. Rei,[79] S. Reid,[32] D. H. Reitze,[1,42] P. Relton,[17] P. Rettegno,[257,52] F. Ricci,[92,47] C. J. Richardson,[35] J. W. Richardson,[1] L. Richardson,[133] P. M. Ricker,[26] G. Riemenschneider,[257,52] K. Riles,[177] M. Rizzo,[15] N. A. Robertson,[1,65] R. Robie,[1] F. Robinet,[40] A. Rocchi,[114] J. A. Rocha,[25] S. Rodriguez,[25] R. D. Rodriguez-Soto,[35] L. Rolland,[48] J. G. Rollins,[1] V. J. Roma,[55] M. Romanelli,[93] R. Romano,[4,5] C. L. Romel,[62] A. Romero,[206] I. M. Romero-Shaw,[6] J. H. Romie,[8] C. A. Rose,[29] D. Rosińska,[97] S. G. Rosofsky,[26] M. P. Ross,[229] S. Rowan,[65] S. J. Rowlinson,[14] Santosh Roy,[3] Soumen Roy,[258] D. Rozza,[111,112] P. Ruggi,[41] K. Ryan,[62] S. Sachdev,[140] T. Sadecki,[62] J. Sadiq,[148] N. Sago,[259] S. Saito,[24] Y. Saito,[184] K. Sakai,[260] Y. Sakai,[188] M. Sakellariadou,[131] Y. Sakuno,[120] O. S. Salafia,[61,60,59] L. Salconi,[41] M. Saleem,[261] F. Salemi,[174,175] A. Samajdar,[49,116] E. J. Sanchez,[1] J. H. Sanchez,[25] L. E. Sanchez,[1] N. Sanchis-Gual,[262] J. R. Sanders,[263] A. Sanuy,[63] T. R. Saravanan,[3] N. Sarin,[6] B. Sassolas,[151] H. Satari,[89] S. Sato,[264] T. Sato,[167] O. Sauter,[42,48] R. L. Savage,[62] V. Savant,[3] T. Sawada,[195] D. Sawant,[94] H. L. Sawant,[3] S. Sayah,[151] D. Schaetzl,[1] M. Scheel,[88] J. Scheuer,[15] A. Schindler-Tyka,[42] P. Schmidt,[14] R. Schnabel,[147] M. Schneewind,[10,11] R. M. S. Schofield,[55] A. Schönbeck,[147] B. W. Schulte,[10,11] B. F. Schutz,[17,10] E. Schwartz,[17] J. Scott,[65] S. M. Scott,[9] M. Seglar-Arroyo,[48] E. Seidel,[26] T. Sekiguchi,[31] Y. Sekiguchi,[265] D. Sellers,[8] A. S. Sengupta,[258] N. Sennett,[100] D. Sentenac,[41] E. G. Seo,[103] V. Sequino,[27,5] A. Sergeev,[209] Y. Setyawati,[10,11] T. Shaffer,[62] M. S. Shahriar,[15] B. Shams,[163] L. Shao,[192] S. Sharifi,[2] A. Sharma,[18,19] P. Sharma,[80] P. Shawhan,[99] N. S. Shcheblanov,[225] H. Shen,[26] S. Shibagaki,[120] M. Shikauchi,[31] R. Shimizu,[24] T. Shimoda,[30] K. Shimode,[184] R. Shink,[221] H. Shinkai,[266] T. Shishido,[46] A. Shoda,[23] D. H. Shoemaker,[66] D. M. Shoemaker,[223] K. Shukla,[186] S. ShyamSundar,[80] M. Sieniawska,[97] D. Sigg,[62] L. P. Singer,[106] D. Singh,[140] N. Singh,[97] A. Singha,[146,49] A. M. Sintes,[136] V. Sipala,[111,112] V. Skliris,[17] B. J. J. Slagmolen,[9] T. J. Slaven-Blair,[89] J. Smetana,[14] J. R. Smith,[25] R. J. E. Smith,[6] S. N. Somala,[267] K. Somiya,[207] E. J. Son,[51] K. Soni,[3] S. Soni,[2] B. Sorazu,[65] V. Sordini,[128] F. Sorrentino,[79] N. Sorrentino,[21,20] H. Sotani,[268] R. Soulard,[87] T. Souradeep,[256,3] E. Sowell,[139] V. Spagnuolo,[146,49] A. P. Spencer,[65] M. Spera,[71,72] A. K. Srivastava,[74] V. Srivastava,[56] K. Staats,[15] C. Stachie,[87] D. A. Steer,[36] J. Steinlechner,[146,49] S. Steinlechner,[146,49] D. J. Stops,[14] M. Stover,[164] K. A. Strain,[65] L. C. Strang,[110] G. Stratta,[269,86] A. Strunk,[62] R. Sturani,[250] A. L. Stuver,[102] J. Südbeck,[147] S. Sudhagar,[3] V. Sudhir,[66] R. Sugimoto,[270,197] H. G. Suh,[29] T. Z. Summerscales,[271] H. Sun,[89] L. Sun,[9,1] S. Sunil,[74] A. Sur,[75] J. Suresh,[31,37] P. J. Sutton,[17] Takamasa Suzuki,[167] Toshikazu Suzuki,[37] B. L. Swinkels,[49] M. J. Szczepańczyk,[42] P. Szewczyk,[97] M. Tacca,[49] H. Tagoshi,[37] S. C. Tait,[65] H. Takahashi,[272] R. Takahashi,[23] A. Takamori,[39] S. Takano,[30] H. Takeda,[30] M. Takeda,[195] C. Talbot,[1] H. Tanaka,[273] Kazuyuki Tanaka,[195] Kenta Tanaka,[273] Taiki Tanaka,[37] Takahiro Tanaka,[259] A. J. Tanasijczuk,[96] S. Tanioka,[23,46] D. B. Tanner,[42] D. Tao,[1] A. Tapia,[25] E. N. Tapia San Martin,[23] E. N. Tapia San Martin,[49] J. D. Tasson,[185] S. Telada,[274] R. Tenorio,[136] L. Terkowski,[147] M. Test,[29] M. P. Thirugnanasambandam,[3] M. Thomas,[8] P. Thomas,[62] J. E. Thompson,[17] S. R. Thondapu,[80] K. A. Thorne,[8] E. Thrane,[6] Shubhanshu Tiwari,[154] Srishti Tiwari,[172] V. Tiwari,[17] K. Toland,[65] A. E. Tolley,[149] T. Tomaru,[23] Y. Tomigami,[195] T. Tomura,[184] M. Tonelli,[21,20] A. Torres-Forné,[117] C. I. Torrie,[1] I. Tosta e Melo,[111,112] D. Töyrä,[9] A. Trapananti,[234,69] F. Travasso,[69,234] G. Traylor,[8] M. C. Tringali,[41] A. Tripathee,[177] L. Troiano,[275,91] A. Trovato,[36] L. Trozzo,[184] R. J. Trudeau,[1] D. S. Tsai,[119] D. Tsai,[119] K. W. Tsang,[49,276,116] T. Tsang,[103] J-S. Tsao,[189] M. Tse,[66] R. Tso,[88] K. Tsubono,[30] S. Tsuchida,[195] L. Tsukada,[31] D. Tsuna,[31] T. Tsutsui,[31] T. Tsuzuki,[24]

M. Turconi,[87] D. Tuyenbayev,[127] A. S. Ubhi,[14] N. Uchikata,[37] T. Uchiyama,[184] R. P. Udall,[101,1] A. Ueda,[179] T. Uehara,[277,278] K. Ueno,[31] G. Ueshima,[279] D. Ugolini,[280] C. S. Unnikrishnan,[172] F. Uraguchi,[24] A. L. Urban,[2] T. Ushiba,[184] S. A. Usman,[124] A. C. Utina,[146,49] H. Vahlbruch,[10,11] G. Vajente,[1] A. Vajpeyi,[6] G. Valdes,[2] M. Valentini,[174,175] V. Valsan,[29] N. van Bakel,[49] M. van Beuzekom,[49] J. F. J. van den Brand,[146,98,49] C. Van Den Broeck,[116,49] D. C. Vander-Hyde,[56] L. van der Schaaf,[49] J. V. van Heijningen,[89,96] J. Vanosky,[1] M. H. P. M. van Putten,[281] M. Vardaro,[227,49] A. F. Vargas,[110] V. Varma,[88] M. Vasúth,[67] A. Vecchio,[14] G. Vedovato,[72] J. Veitch,[65] P. J. Veitch,[77] K. Venkateswara,[229] J. Venneberg,[10,11] G. Venugopalan,[1] D. Verkindt,[48] Y. Verma,[80] D. Veske,[44] F. Vetrano,[85] A. Viceré,[85,86] A. D. Viets,[233] V. Villa-Ortega,[148] J.-Y. Vinet,[87] S. Vitale,[66] T. Vo,[56] H. Vocca,[70,69] E. R. G. von Reis,[62] J. von Wrangel,[10,11] C. Vorvick,[62] S. P. Vyatchanin,[82] L. E. Wade,[164] M. Wade,[164] K. J. Wagner,[118] R. C. Walet,[49] M. Walker,[7] G. S. Wallace,[32] L. Wallace,[1] S. Walsh,[29] J. Wang,[168] J. Z. Wang,[177] W. H. Wang,[142] R. L. Ward,[9] J. Warner,[62] M. Was,[48] T. Washimi,[23] N. Y. Washington,[1] J. Watchi,[137] B. Weaver,[62] L. Wei,[10,11] M. Weinert,[10,11] A. J. Weinstein,[1] R. Weiss,[66] G. Weldon,[177] C. M. Weller,[229] F. Wellmann,[10,11] L. Wen,[89] P. Weßels,[10,11] J. W. Westhouse,[35] K. Wette,[9] J. T. Whelan,[118] D. D. White,[25] B. F. Whiting,[42] C. Whittle,[66] D. Wilken,[10,11] D. Williams,[65] M. J. Williams,[65] A. R. Williamson,[149] J. L. Willis,[1] B. Willke,[10,11] D. J. Wilson,[133] W. Winkler,[10,11] C. C. Wipf,[1] T. Wlodarczyk,[100] G. Woan,[65] J. Woehler,[10,11] J. K. Wofford,[118] I. C. F. Wong,[103] C. Wu,[123] D. S. Wu,[10,11] H. Wu,[123] S. Wu,[123] D. M. Wysocki,[29,118] L. Xiao,[1] W-R. Xu,[189] T. Yamada,[273] H. Yamamoto,[1] Kazuhiro Yamamoto,[183] Kohei Yamamoto,[273] T. Yamamoto,[184] K. Yamashita,[183] R. Yamazaki,[191] F. W. Yang,[163] L. Yang,[158] Yang Yang,[42] Yi Yang,[282] Z. Yang,[58] M. J. Yap,[9] D. W. Yeeles,[17] A. B. Yelikar,[118] M. Ying,[119] K. Yokogawa,[194] J. Yokoyama,[31,30] T. Yokozawa,[184] A. Yoon,[7] T. Yoshioka,[194] Hang Yu,[88] Haocun Yu,[66] H. Yuzurihara,[37] A. Zadrożny,[218] M. Zanolin,[35] S. Zeidler,[283] T. Zelenova,[41] J.-P. Zendri,[72] M. Zevin,[15] M. Zhan,[168] H. Zhang,[189] J. Zhang,[89] L. Zhang,[1] R. Zhang,[42] T. Zhang,[14] C. Zhao,[89] G. Zhao,[137] Yue Zhao,[163] Yuhang Zhao,[23] Z. Zhou,[15] X. J. Zhu,[6] Z.-H. Zhu,[109] M. E. Zucker,[1,66] and J. Zweizig[1]

(LIGO Scientific Collaboration, Virgo Collaboration, and KAGRA Collaboration)

[1]*LIGO Laboratory, California Institute of Technology, Pasadena, California 91125, USA*
[2]*Louisiana State University, Baton Rouge, Louisiana 70803, USA*
[3]*Inter-University Centre for Astronomy and Astrophysics, Pune 411007, India*
[4]*Dipartimento di Farmacia, Università di Salerno, I-84084 Fisciano, Salerno, Italy*
[5]*INFN, Sezione di Napoli, Complesso Universitario di Monte S.Angelo, I-80126 Napoli, Italy*
[6]*OzGrav, School of Physics and Astronomy, Monash University, Clayton 3800, Victoria, Australia*
[7]*Christopher Newport University, Newport News, Virginia 23606, USA*
[8]*LIGO Livingston Observatory, Livingston, Louisiana 70754, USA*
[9]*OzGrav, Australian National University, Canberra, Australian Capital Territory 0200, Australia*
[10]*Max Planck Institute for Gravitational Physics (Albert Einstein Institute), D-30167 Hannover, Germany*
[11]*Leibniz Universität Hannover, D-30167 Hannover, Germany*
[12]*University of Cambridge, Cambridge CB2 1TN, United Kingdom*
[13]*Theoretisch-Physikalisches Institut, Friedrich-Schiller-Universität Jena, D-07743 Jena, Germany*
[14]*University of Birmingham, Birmingham B15 2TT, United Kingdom*
[15]*Center for Interdisciplinary Exploration and Research in Astrophysics (CIERA), Northwestern University, Evanston, Illinois 60208, USA*
[16]*Instituto Nacional de Pesquisas Espaciais, 12227-010 São José dos Campos, São Paulo, Brazil*
[17]*Gravity Exploration Institute, Cardiff University, Cardiff CF24 3AA, United Kingdom*
[18]*Gran Sasso Science Institute (GSSI), I-67100 L'Aquila, Italy*
[19]*INFN, Laboratori Nazionali del Gran Sasso, I-67100 Assergi, Italy*
[20]*INFN, Sezione di Pisa, I-56127 Pisa, Italy*
[21]*Università di Pisa, I-56127 Pisa, Italy*
[22]*International Centre for Theoretical Sciences, Tata Institute of Fundamental Research, Bengaluru 560089, India*
[23]*Gravitational Wave Science Project, National Astronomical Observatory of Japan (NAOJ), Mitaka City, Tokyo 181-8588, Japan*
[24]*Advanced Technology Center, National Astronomical Observatory of Japan (NAOJ), Mitaka City, Tokyo 181-8588, Japan*
[25]*California State University Fullerton, Fullerton, California 92831, USA*
[26]*NCSA, University of Illinois at Urbana-Champaign, Urbana, Illinois 61801, USA*
[27]*Università di Napoli "Federico II", Complesso Universitario di Monte S.Angelo, I-80126 Napoli, Italy*

[28]Université de Lyon, Université Claude Bernard Lyon 1, CNRS, Institut Lumière Matière, F-69622 Villeurbanne, France
[29]University of Wisconsin-Milwaukee, Milwaukee, Wisconsin 53201, USA
[30]Department of Physics, The University of Tokyo, Bunkyo-ku, Tokyo 113-0033, Japan
[31]Research Center for the Early Universe (RESCEU), The University of Tokyo, Bunkyo-ku, Tokyo 113-0033, Japan
[32]SUPA, University of Strathclyde, Glasgow G1 1XQ, United Kingdom
[33]Dipartimento di Matematica e Informatica, Università di Udine, I-33100 Udine, Italy
[34]INFN, Sezione di Trieste, I-34127 Trieste, Italy
[35]Embry-Riddle Aeronautical University, Prescott, Arizona 86301, USA
[36]Université de Paris, CNRS, Astroparticule et Cosmologie, F-75006 Paris, France
[37]Institute for Cosmic Ray Research (ICRR), KAGRA Observatory, The University of Tokyo, Kashiwa City, Chiba 277-8582, Japan
[38]Accelerator Laboratory, High Energy Accelerator Research Organization (KEK), Tsukuba City, Ibaraki 305-0801, Japan
[39]Earthquake Research Institute, The University of Tokyo, Bunkyo-ku, Tokyo 113-0032, Japan
[40]Université Paris-Saclay, CNRS/IN2P3, IJCLab, 91405 Orsay, France
[41]European Gravitational Observatory (EGO), I-56021 Cascina, Pisa, Italy
[42]University of Florida, Gainesville, Florida 32611, USA
[43]Department of Mathematics and Physics, Hirosaki University, Hirosaki City, Aomori 036-8561, Japan
[44]Columbia University, New York, New York 10027, USA
[45]Kamioka Branch, National Astronomical Observatory of Japan (NAOJ), Kamioka-cho, Hida City, Gifu 506-1205, Japan
[46]The Graduate University for Advanced Studies (SOKENDAI), Mitaka City, Tokyo 181-8588, Japan
[47]INFN, Sezione di Roma, I-00185 Roma, Italy
[48]Univ. Grenoble Alpes, Laboratoire d'Annecy de Physique des Particules (LAPP), Université Savoie Mont Blanc, CNRS/IN2P3, F-74941 Annecy, France
[49]Nikhef, Science Park 105, 1098 XG Amsterdam, Netherlands
[50]Korea Institute of Science and Technology Information (KISTI), Yuseong-gu, Daejeon 34141, Korea
[51]National Institute for Mathematical Sciences, Daejeon 34047, South Korea
[52]INFN Sezione di Torino, I-10125 Torino, Italy
[53]International College, Osaka University, Toyonaka City, Osaka 560-0043, Japan
[54]School of High Energy Accelerator Science, The Graduate University for Advanced Studies (SOKENDAI), Tsukuba City, Ibaraki 305-0801, Japan
[55]University of Oregon, Eugene, Oregon 97403, USA
[56]Syracuse University, Syracuse, New York 13244, USA
[57]Université de Liège, B-4000 Liège, Belgium
[58]University of Minnesota, Minneapolis, Minnesota 55455, USA
[59]Università degli Studi di Milano-Bicocca, I-20126 Milano, Italy
[60]INFN, Sezione di Milano-Bicocca, I-20126 Milano, Italy
[61]INAF, Osservatorio Astronomico di Brera sede di Merate, I-23807 Merate, Lecco, Italy
[62]LIGO Hanford Observatory, Richland, Washington 99352, USA
[63]Institut de Ciències del Cosmos, Universitat de Barcelona, C/ Martí i Franquès 1, Barcelona, 08028, Spain
[64]Dipartimento di Medicina, Chirurgia e Odontoiatria "Scuola Medica Salernitana", Università di Salerno, I-84081 Baronissi, Salerno, Italy
[65]SUPA, University of Glasgow, Glasgow G12 8QQ, United Kingdom
[66]LIGO Laboratory, Massachusetts Institute of Technology, Cambridge, Massachusetts 02139, USA
[67]Wigner RCP, RMKI, H-1121 Budapest, Konkoly Thege Miklós út 29-33, Hungary
[68]Stanford University, Stanford, California 94305, USA
[69]INFN, Sezione di Perugia, I-06123 Perugia, Italy
[70]Università di Perugia, I-06123 Perugia, Italy
[71]Università di Padova, Dipartimento di Fisica e Astronomia, I-35131 Padova, Italy
[72]INFN, Sezione di Padova, I-35131 Padova, Italy
[73]Montana State University, Bozeman, Montana 59717, USA
[74]Institute for Plasma Research, Bhat, Gandhinagar 382428, India
[75]Nicolaus Copernicus Astronomical Center, Polish Academy of Sciences, 00-716, Warsaw, Poland
[76]Dipartimento di Ingegneria, Università del Sannio, I-82100 Benevento, Italy
[77]OzGrav, University of Adelaide, Adelaide, South Australia 5005, Australia
[78]California State University, Los Angeles, 5151 State University Dr, Los Angeles, California 90032, USA

[79]*INFN, Sezione di Genova, I-16146 Genova, Italy*
[80]*RRCAT, Indore, Madhya Pradesh 452013, India*
[81]*Missouri University of Science and Technology, Rolla, Missouri 65409, USA*
[82]*Faculty of Physics, Lomonosov Moscow State University, Moscow 119991, Russia*
[83]*SUPA, University of the West of Scotland, Paisley PA1 2BE, United Kingdom*
[84]*Bar-Ilan University, Ramat Gan, 5290002, Israel*
[85]*Università degli Studi di Urbino "Carlo Bo", I-61029 Urbino, Italy*
[86]*INFN, Sezione di Firenze, I-50019 Sesto Fiorentino, Firenze, Italy*
[87]*Artemis, Université Côte d'Azur, Observatoire de la Côte d'Azur, CNRS, F-06304 Nice, France*
[88]*CaRT, California Institute of Technology, Pasadena, California 91125, USA*
[89]*OzGrav, University of Western Australia, Crawley, Western Australia 6009, Australia*
[90]*Dipartimento di Fisica "E.R. Caianiello", Università di Salerno, I-84084 Fisciano, Salerno, Italy*
[91]*INFN, Sezione di Napoli, Gruppo Collegato di Salerno, Complesso Universitario di Monte S. Angelo, I-80126 Napoli, Italy*
[92]*Università di Roma "La Sapienza", I-00185 Roma, Italy*
[93]*Univ Rennes, CNRS, Institut FOTON—UMR6082, F-3500 Rennes, France*
[94]*Indian Institute of Technology Bombay, Powai, Mumbai 400 076, India*
[95]*Laboratoire Kastler Brossel, Sorbonne Université, CNRS, ENS-Université PSL, Collège de France, F-75005 Paris, France*
[96]*Université catholique de Louvain, B-1348 Louvain-la-Neuve, Belgium*
[97]*Astronomical Observatory Warsaw University, 00-478 Warsaw, Poland*
[98]*VU University Amsterdam, 1081 HV Amsterdam, Netherlands*
[99]*University of Maryland, College Park, Maryland 20742, USA*
[100]*Max Planck Institute for Gravitational Physics (Albert Einstein Institute), D-14476 Potsdam, Germany*
[101]*School of Physics, Georgia Institute of Technology, Atlanta, Georgia 30332, USA*
[102]*Villanova University, 800 Lancaster Ave, Villanova, Pennsylvania 19085, USA*
[103]*Faculty of Science, Department of Physics, The Chinese University of Hong Kong, Shatin, N.T., Hong Kong*
[104]*Stony Brook University, Stony Brook, New York 11794, USA*
[105]*Center for Computational Astrophysics, Flatiron Institute, New York, New York 10010, USA*
[106]*NASA Goddard Space Flight Center, Greenbelt, Maryland 20771, USA*
[107]*Dipartimento di Fisica, Università degli Studi di Genova, I-16146 Genova, Italy*
[108]*Tsinghua University, Beijing 100084, China*
[109]*Department of Astronomy, Beijing Normal University, Beijing 100875, China*
[110]*OzGrav, University of Melbourne, Parkville, Victoria 3010, Australia*
[111]*Università degli Studi di Sassari, I-07100 Sassari, Italy*
[112]*INFN, Laboratori Nazionali del Sud, I-95125 Catania, Italy*
[113]*Università di Roma Tor Vergata, I-00133 Roma, Italy*
[114]*INFN, Sezione di Roma Tor Vergata, I-00133 Roma, Italy*
[115]*University of Sannio at Benevento, I-82100 Benevento, Italy and INFN, Sezione di Napoli, I-80100 Napoli, Italy*
[116]*Institute for Gravitational and Subatomic Physics (GRASP), Utrecht University, Princetonplein 1, 3584 CC Utrecht, Netherlands*
[117]*Departamento de Astronomía y Astrofísica, Universitat de València, E-46100 Burjassot, València, Spain*
[118]*Rochester Institute of Technology, Rochester, New York 14623, USA*
[119]*National Tsing Hua University, Hsinchu City, 30013 Taiwan, Republic of China*
[120]*Department of Applied Physics, Fukuoka University, Jonan, Fukuoka City, Fukuoka 814-0180, Japan*
[121]*OzGrav, Charles Sturt University, Wagga Wagga, New South Wales 2678, Australia*
[122]*Department of Physics, Tamkang University, Danshui Dist., New Taipei City 25137, Taiwan*
[123]*Department of Physics and Institute of Astronomy, National Tsing Hua University, Hsinchu 30013, Taiwan*
[124]*University of Chicago, Chicago, Illinois 60637, USA*
[125]*Department of Physics, Center for High Energy and High Field Physics, National Central University, Zhongli District, Taoyuan City 32001, Taiwan*
[126]*Dipartimento di Ingegneria Industriale (DIIN), Università di Salerno, I-84084 Fisciano, Salerno, Italy*
[127]*Institute of Physics, Academia Sinica, Nankang, Taipei 11529, Taiwan*
[128]*Institut de Physique des 2 Infinis de Lyon (IP2I), CNRS/IN2P3, Université de Lyon, Université Claude Bernard Lyon 1, F-69622 Villeurbanne, France*
[129]*Seoul National University, Seoul 08826, South Korea*

[130]Pusan National University, Busan 46241, South Korea
[131]King's College London, University of London, London WC2R 2LS, United Kingdom
[132]INAF, Osservatorio Astronomico di Padova, I-35122 Padova, Italy
[133]University of Arizona, Tucson, Arizona 85721, USA
[134]Rutherford Appleton Laboratory, Didcot OX11 0DE, United Kingdom
[135]Université libre de Bruxelles, Avenue Franklin Roosevelt 50—1050 Bruxelles, Belgium
[136]Universitat de les Illes Balears, IAC3—IEEC, E-07122 Palma de Mallorca, Spain
[137]Université Libre de Bruxelles, Brussels 1050, Belgium
[138]Departamento de Matemáticas, Universitat de València, E-46100 Burjassot, València, Spain
[139]Texas Tech University, Lubbock, Texas 79409, USA
[140]The Pennsylvania State University, University Park, Pennsylvania 16802, USA
[141]University of Rhode Island, Kingston, Rhode Island 02881, USA
[142]The University of Texas Rio Grande Valley, Brownsville, Texas 78520, USA
[143]Bellevue College, Bellevue, Washington 98007, USA
[144]Scuola Normale Superiore, Piazza dei Cavalieri, 7—56126 Pisa, Italy
[145]MTA-ELTE Astrophysics Research Group, Institute of Physics, Eötvös University, Budapest 1117, Hungary
[146]Maastricht University, 6200 MD, Maastricht, Netherlands
[147]Universität Hamburg, D-22761 Hamburg, Germany
[148]IGFAE, Campus Sur, Universidade de Santiago de Compostela, 15782 Spain
[149]University of Portsmouth, Portsmouth, PO1 3FX, United Kingdom
[150]The University of Sheffield, Sheffield S10 2TN, United Kingdom
[151]Laboratoire des Matériaux Avancés (LMA), Institut de Physique des 2 Infinis (IP2I) de Lyon, CNRS/IN2P3, Université de Lyon, Université Claude Bernard Lyon 1, F-69622 Villeurbanne, France
[152]Dipartimento di Scienze Matematiche, Fisiche e Informatiche, Università di Parma, I-43124 Parma, Italy
[153]INFN, Sezione di Milano Bicocca, Gruppo Collegato di Parma, I-43124 Parma, Italy
[154]Physik-Institut, University of Zurich, Winterthurerstrasse 190, 8057 Zurich, Switzerland
[155]Université de Strasbourg, CNRS, IPHC UMR 7178, F-67000 Strasbourg, France
[156]West Virginia University, Morgantown, West Virginia 26506, USA
[157]Montclair State University, Montclair, New Jersey 07043, USA
[158]Colorado State University, Fort Collins, Oregon 80523, USA
[159]Institute for Nuclear Research, Hungarian Academy of Sciences, Bem t'er 18/c, H-4026 Debrecen, Hungary
[160]CNR-SPIN, c/o Università di Salerno, I-84084 Fisciano, Salerno, Italy
[161]Scuola di Ingegneria, Università della Basilicata, I-85100 Potenza, Italy
[162]Observatori Astronòmic, Universitat de València, E-46980 Paterna, València, Spain
[163]The University of Utah, Salt Lake City, Utah 84112, USA
[164]Kenyon College, Gambier, Ohio 43022, USA
[165]Vrije Universiteit Amsterdam, 1081 HV, Amsterdam, Netherlands
[166]Department of Astronomy, The University of Tokyo, Mitaka City, Tokyo 181-8588, Japan
[167]Faculty of Engineering, Niigata University, Nishi-ku, Niigata City, Niigata 950-2181, Japan
[168]State Key Laboratory of Magnetic Resonance and Atomic and Molecular Physics, Innovation Academy for Precision Measurement Science and Technology (APM), Chinese Academy of Sciences, Xiao Hong Shan, Wuhan 430071, China
[169]University of Szeged, Dóm tér 9, Szeged 6720, Hungary
[170]Universiteit Gent, B-9000 Gent, Belgium
[171]University of British Columbia, Vancouver, British Columbia V6T 1Z4, Canada
[172]Tata Institute of Fundamental Research, Mumbai 400005, India
[173]INAF, Osservatorio Astronomico di Capodimonte, I-80131 Napoli, Italy
[174]Università di Trento, Dipartimento di Fisica, I-38123 Povo, Trento, Italy
[175]INFN, Trento Institute for Fundamental Physics and Applications, I-38123 Povo, Trento, Italy
[176]The University of Mississippi, University, Mississippi 38677, USA
[177]University of Michigan, Ann Arbor, Michigan 48109, USA
[178]Department of Physics, School of Natural Science, Ulsan National Institute of Science and Technology (UNIST), Ulju-gun, Ulsan 44919, Korea
[179]Applied Research Laboratory, High Energy Accelerator Research Organization (KEK), Tsukuba City, Ibaraki 305-0801, Japan
[180]Dipartimento di Fisica, Università di Trieste, I-34127 Trieste, Italy
[181]Shanghai Astronomical Observatory, Chinese Academy of Sciences, Shanghai 200030, China

[182]*American University, Washington, D.C. 20016, USA*
[183]*Faculty of Science, University of Toyama, Toyama City, Toyama 930-8555, Japan*
[184]*Institute for Cosmic Ray Research (ICRR), KAGRA Observatory, The University of Tokyo, Kamioka-cho, Hida City, Gifu 506-1205, Japan*
[185]*Carleton College, Northfield, Minnesota 55057, USA*
[186]*University of California, Berkeley, California 94720, USA*
[187]*College of Industrial Technology, Nihon University, Narashino City, Chiba 275-8575, Japan*
[188]*Graduate School of Science and Technology, Niigata University, Nishi-ku, Niigata City, Niigata 950-2181, Japan*
[189]*Department of Physics, National Taiwan Normal University, sec. IV, Taipei 116, Taiwan*
[190]*Astronomy and Space Science, Chungnam National University, Yuseong-gu, Daejeon 34134, Korea, Korea*
[191]*Department of Physics and Mathematics, Aoyama Gakuin University, Sagamihara City, Kanagawa 252-5258, Japan*
[192]*Kavli Institute for Astronomy and Astrophysics, Peking University, Haidian District, Beijing 100871, China*
[193]*Yukawa Institute for Theoretical Physics (YITP), Kyoto University, Sakyou-ku, Kyoto City, Kyoto 606-8502, Japan*
[194]*Graduate School of Science and Engineering, University of Toyama, Toyama City, Toyama 930-8555, Japan*
[195]*Department of Physics, Graduate School of Science, Osaka City University, Sumiyoshi-ku, Osaka City, Osaka 558-8585, Japan*
[196]*Nambu Yoichiro Institute of Theoretical and Experimental Physics (NITEP), Osaka City University, Sumiyoshi-ku, Osaka City, Osaka 558-8585, Japan*
[197]*Institute of Space and Astronautical Science (JAXA), Chuo-ku, Sagamihara City, Kanagawa 252-0222, Japan*
[198]*Directorate of Construction, Services and Estate Management, Mumbai 400094 India*
[199]*Universiteit Antwerpen, Prinsstraat 13, 2000 Antwerpen, Belgium*
[200]*University of Białystok, 15-424 Białystok, Poland*
[201]*Department of Physics, Ewha Womans University, Seodaemun-gu, Seoul 03760, Korea*
[202]*National Astronomical Observatories, Chinese Academic of Sciences, Chaoyang District, Beijing, China*
[203]*School of Astronomy and Space Science, University of Chinese Academy of Sciences, Chaoyang District, Beijing, China*
[204]*University of Southampton, Southampton SO17 1BJ, United Kingdom*
[205]*Institute for Cosmic Ray Research (ICRR), The University of Tokyo, Kashiwa City, Chiba 277-8582, Japan*
[206]*Institut de Física d'Altes Energies (IFAE), Barcelona Institute of Science and Technology, and ICREA, E-08193 Barcelona, Spain*
[207]*Graduate School of Science and Technology, Tokyo Institute of Technology, Meguro-ku, Tokyo 152-8551, Japan*
[208]*University of Washington Bothell, Bothell, Washington 98011, USA*
[209]*Institute of Applied Physics, Nizhny Novgorod, 603950, Russia*
[210]*Ewha Womans University, Seoul 03760, South Korea*
[211]*Inje University Gimhae, South Gyeongsang 50834, South Korea*
[212]*Department of Physics, Myongji University, Yongin 17058, Korea*
[213]*Korea Astronomy and Space Science Institute (KASI), Yuseong-gu, Daejeon 34055, Korea*
[214]*Department of Physical Science, Hiroshima University, Higashihiroshima City, Hiroshima 903-0213, Japan*
[215]*Bard College, 30 Campus Rd, Annandale-On-Hudson, New York 12504, USA*
[216]*Institute for Cosmic Ray Research (ICRR), Research Center for Cosmic Neutrinos (RCCN), The University of Tokyo, Kamioka-cho, Hida City, Gifu 506-1205, Japan*
[217]*Institute of Mathematics, Polish Academy of Sciences, 00656 Warsaw, Poland*
[218]*National Center for Nuclear Research, 05-400 Świerk-Otwock, Poland*
[219]*Cornell University, Ithaca, New York 14850, USA*
[220]*Institute for Advanced Research, Nagoya University, Furocho, Chikusa-ku, Nagoya City, Aichi 464-8602, Japan*
[221]*Université de Montréal/Polytechnique, Montreal, Quebec H3T 1J4, Canada*
[222]*Laboratoire Lagrange, Université Côte d'Azur, Observatoire Côte d'Azur, CNRS, F-06304 Nice, France*

[223]Department of Physics, University of Texas, Austin, Texas 78712, USA
[224]Department of Physics, Hanyang University, Seoul 04763, Korea
[225]NAVIER, École des Ponts, Univ Gustave Eiffel, CNRS, Marne-la-Vallée, France
[226]National Center for High-performance computing, National Applied Research Laboratories, Hsinchu Science Park, Hsinchu City 30076, Taiwan
[227]Institute for High-Energy Physics, University of Amsterdam, Science Park 904, 1098 XH Amsterdam, Netherlands
[228]NASA Marshall Space Flight Center, Huntsville, Alabama 35811, USA
[229]University of Washington, Seattle, Washington 98195, USA
[230]Dipartimento di Matematica e Fisica, Università degli Studi Roma Tre, I-00146 Roma, Italy
[231]INFN, Sezione di Roma Tre, I-00146 Roma, Italy
[232]ESPCI, CNRS, F-75005 Paris, France
[233]Concordia University Wisconsin, Mequon, Wisconsin 53097, USA
[234]Università di Camerino, Dipartimento di Fisica, I-62032 Camerino, Italy
[235]Southern University and A&M College, Baton Rouge, Louisiana 70813, USA
[236]Centre Scientifique de Monaco, 8 quai Antoine Ier, MC-98000, Monaco
[237]Institute for Photon Science and Technology, The University of Tokyo, Bunkyo-ku, Tokyo 113-8656, Japan
[238]Indian Institute of Technology Madras, Chennai 600036, India
[239]Saha Institute of Nuclear Physics, Bidhannagar, West Bengal 700064, India
[240]The Applied Electromagnetic Research Institute, National Institute of Information and Communications Technology (NICT), Koganei City, Tokyo 184-8795, Japan
[241]Institut des Hautes Etudes Scientifiques, F-91440 Bures-sur-Yvette, France
[242]Faculty of Law, Ryukoku University, Fushimi-ku, Kyoto City, Kyoto 612-8577, Japan
[243]Indian Institute of Science Education and Research, Kolkata, Mohanpur, West Bengal 741252, India
[244]Department of Astrophysics/IMAPP, Radboud University Nijmegen, P.O. Box 9010, 6500 GL Nijmegen, Netherlands
[245]Department of Physics, University of Notre Dame, Notre Dame, Indiana 46556, USA
[246]Department of Physics, National Tsing Hua University, Hsinchu 30013, Taiwan
[247]GRAPPA, Anton Pannekoek Institute for Astronomy and Institute for High-Energy Physics, University of Amsterdam, Science Park 904, 1098 XH Amsterdam, Netherlands
[248]Consiglio Nazionale delle Ricerche—Istituto dei Sistemi Complessi, Piazzale Aldo Moro 5, I-00185 Roma, Italy
[249]Hobart and William Smith Colleges, Geneva, New York 14456, USA
[250]International Institute of Physics, Universidade Federal do Rio Grande do Norte, Natal RN 59078-970, Brazil
[251]Museo Storico della Fisica e Centro Studi e Ricerche "Enrico Fermi", I-00184 Roma, Italy
[252]Department of Engineering, University of Sannio, Benevento 82100, Italy
[253]Lancaster University, Lancaster LA1 4YW, United Kingdom
[254]OzGrav, Swinburne University of Technology, Hawthorn Victoria 3122, Australia
[255]Università di Trento, Dipartimento di Matematica, I-38123 Povo, Trento, Italy
[256]Indian Institute of Science Education and Research, Pune, Maharashtra 411008, India
[257]Dipartimento di Fisica, Università degli Studi di Torino, I-10125 Torino, Italy
[258]Indian Institute of Technology, Palaj, Gandhinagar, Gujarat 382355, India
[259]Department of Physics, Kyoto University, Sakyou-ku, Kyoto City, Kyoto 606-8502, Japan
[260]Department of Electronic Control Engineering, National Institute of Technology, Nagaoka College, Nagaoka City, Niigata 940-8532, Japan
[261]Chennai Mathematical Institute, Chennai 603103, India
[262]Centro de Astrofísica e Gravitação (CENTRA), Departamento de Física, Instituto Superior Técnico, Universidade de Lisboa, 1049-001 Lisboa, Portugal
[263]Marquette University, 11420 W. Clybourn St., Milwaukee, Wisconsin 53233, USA
[264]Graduate School of Science and Engineering, Hosei University, Koganei City, Tokyo 184-8584, Japan
[265]Faculty of Science, Toho University, Funabashi City, Chiba 274-8510, Japan
[266]Faculty of Information Science and Technology, Osaka Institute of Technology, Hirakata City, Osaka 573-0196, Japan
[267]Indian Institute of Technology Hyderabad, Sangareddy, Khandi, Telangana 502285, India
[268]iTHEMS (Interdisciplinary Theoretical and Mathematical Sciences Program), The Institute of Physical and Chemical Research (RIKEN), Wako, Saitama 351-0198, Japan
[269]INAF, Osservatorio di Astrofisica e Scienza dello Spazio, I-40129 Bologna, Italy

[270]*Department of Space and Astronautical Science, The Graduate University for Advanced Studies (SOKENDAI), Sagamihara, Kanagawa 252-5210, Japan*
[271]*Andrews University, Berrien Springs, Michigan 49104, USA*
[272]*Research Center for Space Science, Advanced Research Laboratories, Tokyo City University, Setagaya, Tokyo 158-0082, Japan*
[273]*Institute for Cosmic Ray Research (ICRR), Research Center for Cosmic Neutrinos (RCCN), The University of Tokyo, Kashiwa City, Chiba 277-8582, Japan*
[274]*National Metrology Institute of Japan, National Institute of Advanced Industrial Science and Technology, Tsukuba City, Ibaraki 305-8568, Japan*
[275]*Dipartimento di Scienze Aziendali—Management and Innovation Systems (DISA-MIS), Università di Salerno, I-84084 Fisciano, Salerno, Italy*
[276]*Van Swinderen Institute for Particle Physics and Gravity, University of Groningen, Nijenborgh 4, 9747 AG Groningen, Netherlands*
[277]*Department of Communications Engineering, National Defense Academy of Japan, Yokosuka City, Kanagawa 239-8686, Japan*
[278]*Department of Physics, University of Florida, Gainesville, Florida 32611, USA*
[279]*Department of Information and Management Systems Engineering, Nagaoka University of Technology, Nagaoka City, Niigata 940-2188, Japan*
[280]*Trinity University, San Antonio, Texas 78212, USA*
[281]*Department of Physics and Astronomy, Sejong University, Gwangjin-gu, Seoul 143-747, Korea*
[282]*Department of Electrophysics, National Chiao Tung University, Hsinchu, Taiwan*
[283]*Department of Physics, Rikkyo University, Toshima-ku, Tokyo 171-8501, Japan*

[a]Deceased.